Chapter 2: Solar Ultra-violet Visible and IR Telescope

2.1. Introduction

2.1.1. Solar UV-Visible-IR telescope in SOLAR-C Plan-B

The emergence of magnetic fields, its forcing by convective flows on the solar surface, and its interaction with previously-emerged magnetic flux, give rise to energetic phenomena in the solar atmosphere through magneto-hydrodynamic processes. The Hinode Solar Optical Telescope (SOT) now provides the first high-resolution diagnostics of the solar magnetic field from a space platform, and now allows discovering the processes by which magnetic flux interacts with the convective flows in the lower solar atmosphere, “photosphere”. Furthermore, Hinode and recent ground-based telescopes has provided strong indications that those photospheric dynamics initiate outward propagating waves and dynamic reconnection events that result in acceleration and heating of the plasma accompanied by significant outward energy and mass flux in the upper atmosphere, i.e. “chromosphere” and “corona”. Unfortunately, our knowledge on the magnetism of the solar chromosphere is practically inexistent notwithstanding the qualitative information provided by monochromatic images at various spectral lines sensitive to the chromosphere. Such intensity images do not provide any quantitative information on the temperatures, velocities, and magnetic fields.

In these circumstances, the primary objective of the instrument, Solar Ultra-violet Visible and IR telescope (SUVIT), is to explore dynamical nature of the magnetic solar atmosphere and physical processes responsible for making the dynamics through spectroscopic and polarimetric measurements of physical conditions (e.g. temperatures and velocities) with emphasis on magnetic fields in the chromosphere. Quantitative information on magnetic fields in the place where magnetic energies are transferred and liberated is critically important to expand our knowledge on the magnetized atmosphere although it has been significant challenges in measuring magnetic fields above the photosphere because of lower polarization signals in spectrum lines emanating from the chromosphere.

The observations also demand parallel efforts in advanced data analysis, interpretation, and modeling methods. Fortunately, at present we live in a time where rapid advancement in the analysis and modeling are taking place, and the models describe their synthetic chromosphere/corona with increasing realism (see Appendix A.3 and A.4). These theoretical advances demand new observational constraints. The present concept of SUVIT is structured to provide those specific observational constraints.

2.1.2. Science targets with the instrument

- *Magnetized solar atmospheres: how they are created and evolve.*

Hinode has demonstrated that a space-based telescope has strong benefits in precise spectro-polarimetric observations. It allows studying structures and dynamics in the photosphere, such as formation of strong flux concentration, its interaction with granular convection, and sunspots structures and dynamics associated with strong magneto-convection. The next step is to extend our quantitative knowledge of the solar atmosphere from the photosphere to the chromosphere (Fig. 2.1). In the chromosphere, magnetic pressure becomes comparable with or dominant over gas pressure (i.e. plasma beta≤ 1) while gas pressure is dominating in the photosphere. This is why measurements of magnetic fields in the atmospheric layer higher than the photosphere is demanded, which also helps to infer magnetic field configuration in coronae through magnetic field extrapolation such as potential field and force-free field modeling.

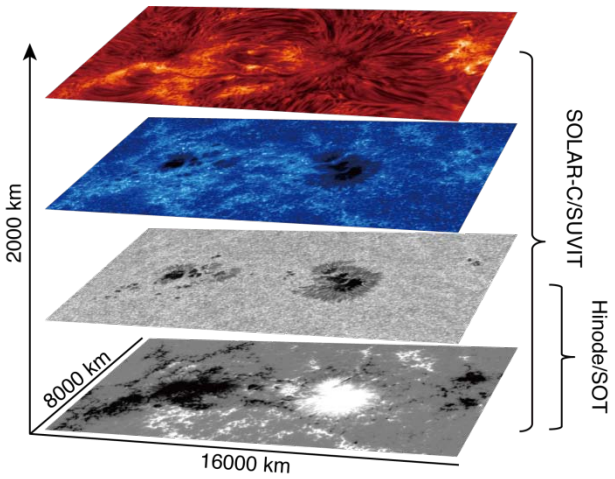

Fig. 2.1. SUVIT on SOLAR-C extends our quantitative knowledge on the magnetized solar atmosphere from the photosphere to the chromosphere.

In the quiet Sun, granular-scale horizontal field emergences are ubiquitously found in the photosphere, which were extensively studied using Hinode (Lites et al. 2008, Centeno et al. 2007, Orozco Suarez et al. 2007, Ishikawa et al. 2008). An outstanding question is how much fraction of magnetic fields keep expanding into the upper atmospheres, and how they are reconfigured to create canopy structures overlying the quiet photosphere. The observations are truly essential to know eventual history of emergent magnetic fields. High-resolution observations with Hinode and recent ground-based telescope showed super-sonic upflows and downflows ubiquitously seen at the photospheric layer. Some of them are associated with formation of strong flux tubes (e.g. Nagata et al. 2008), and some of them are associated with cancellation or disappearance of bipolar magnetic flux (e.g. Kubo et al. 2010). Driving mechanisms and ultimate consequence of the flows could be physically interpreted with SUVIT owing to combined measurements of plasma properties and magnetic fields at the multiple atmospheric layers.

A solar prominence is also an important target with SUVIT because it carries significant amount of magnetic flux and masses in coronal mass ejections (CME). In spite of the importance, its magnetic field configuration is poorly known. This is primarily because of lack of observational information on magnetic field configuration in the prominence. Hinode SOT observations revealed that structures in prominences are very complicated in the spatial scale smaller than 1000 km (Okamoto et al. 2007,

Berger et al. 2008). It is essential to understand how the fine scale structures are created and how cool materials are provided and sustained in the upper atmosphere. There are some observations of field emergence at the photospheric layer with Hinode (Okamoto et al. 2009, Lites et al. 2010), but long-term observations of the photospheric and chromospheric fields with SUVIT provide an entirely new view on formation and evolution processes of the prominences.

- *Small-scale dynamic phenomena responsible for the energy transfer.*

One of the science goals of the Solar-C plan-B is to elucidate the energy and mass transfer from the photosphere upward through the chromosphere to the corona. Although the chromosphere occupies only a very thin region in physical dimensions relative to the structure of the overlying corona, it is the region where most of the non-radiative heating takes place, and it forms the conduit for the upward flux of mass and energy.

Significant progress has already been realized in understanding the chromosphere (Fig. 2.2). Above the very quiet photospheric internetwork where the magnetic field is weakest, the chromosphere is dominated by largely acoustic shocks initiated in the photosphere and below by action of the solar convection and the p-mode oscillations (Carlsson and Stein 1997, Rutten 2007). Recent observations from Hinode and other instruments have suggested that the network fields, interacting with convection, energize and structure the chromosphere. In particular, the “type II spicules” now appear to be a candidate for channeling the upward movement of mass and energy toward the corona (De Pontieu et al. 2011). Active phenomena in the chromosphere increase within active regions, where outward propagating jets, such as chromospheric micro-jets in penumbrae (Katsukawa et al. 2007), Ellerman bombs (Georgoulis et al. 2002) and chromospheric jets (Shibata et al. 2007) around sunspots, occur frequently. In most of the active phenomena in the chromosphere, magnetic reconnection is suggested to play an essential role to energize the outward flow. But there have been no direct measurements of magnetic field configuration around the reconnection site. High-resolution observations from SUVIT would provide observations of the chromospheric magnetic field in and around these active chromospheric phenomena, and also provide the accompanying thermodynamic conditions therein. It is demanded to get knowledge on what the condition is to trigger the magnetic reconnection and how fast it dissipates magnetic energies.

Energy transfer between the atmospheric layers takes place through not only radiation and flows, but also propagation of magneto-hydrodynamic (MHD) waves. Though it has been difficult to catch signatures of waves in observational data, transverse oscillation of chromospheric structures are now ubiquitously discovered in imaging observations with Hinode thanks to its high and stable image quality (Okamoto et al. 2007, De Pontieu et al. 2007). In the photosphere signatures of propagation and reflection of MHD waves are found in spectro-polarimetric observations (Fujimura and Tsuneta 2009). Quantitative measurements of fluctuations in magnetic fields and thermodynamic parameters are essential to understand how and where the waves are generated, reflected, and dissipated. Especially it is important to know nature of waves by identifying MHD wave modes and mode conversion for subsequent shock formation, resulting in plasma heating.

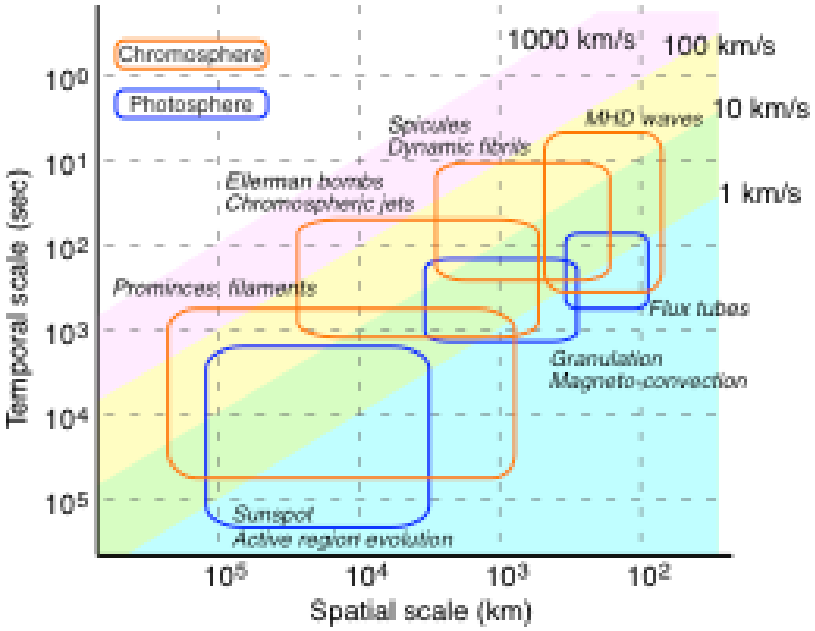

Fig. 2.2. Structures and dynamics seen in the photosphere and the chromosphere. In the chromosphere, lots of dynamics are taking place in the broad spatial and temporal range. Velocities of waves and flows are typically 10 – 100 km/s, one order of magnitude faster than typical velocities seen in the photosphere.

2.2. Basic requirements to the instrument

The science targets described above leads to basic requirements to the instrument as summarized below:

- *Polarimetric sensitivity and accuracy*

The polarimetric sensitivity in Hinode/SOT and existing ground–based telescope is typically ~10^{-3}, which is enough to get polarization signals with photospheric lines but marginal to detect the polarization signals in the chromospheric lines. For detailed measurements of the circular polarized profiles induced by the longitudinal Zeeman effect and linear polarized profiles induced by the Zeeman and Hanle effect in the field strength down to 10 gauss, we need the sensitivity of at least 10^{-4} (see A.2 and Fig. 2.23), which means we have to collect at least 10^8 photons when the sensitivity is limited with photon noise. In order to collect the number of photons with 0.2” spatial sampling and 10 to 20 sec temporal sampling, we need an aperture diameter larger than 1 m (see Fig. 2.3). It is necessary to have a strategy to minimize instrumental polarization and to remove residual polarization cross-talk with pre-flight and in-flight calibration to achieve high polarimetric accuracy.

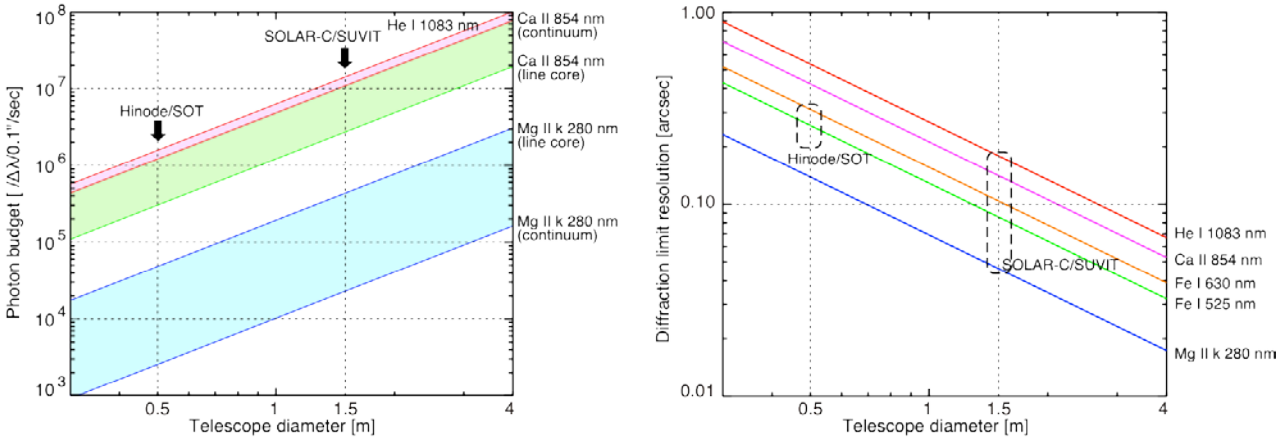

Fig. 2.3. Collectable number of photons as a function of the telescope diameter at major chromospheric lines (*right*). It is assumed that the overall efficiency of the instrument is 0.1 with the spatial sampling of 0.1", the temporal sampling of 1 sec, and the wavelength sampling of $\Delta\lambda/\lambda=2\text{x}10^5$. Diffraction-limited spatial resolution as a function of the telescope diameter (*left*).

- *Spatial resolution*

In order to resolve the structures in the chromospheres such as spicules and fibrils, whose spatial scale is smaller than 0.2", and also to detect small amplitudes of magneto-hydrodynamic waves and changes of magnetic fields associated with magnetic reconnection taking place inside the chromospheric structures, we need 0.1" resolution at the shortest wavelength (Fig. 2.2) and diffraction-limited resolution in the wavelength range longer than visible lights (0.18" at 1.1 μm in the case of φ 1.5 m, Fig. 2.3). In order to collect plenty number of photons required for the polarimetric sensitivity of 10^{-4}, we might have to mitigate the spatial sampling while keeping spatial sampling of 0.2" to 0.3" required to dissolve the elemental chromospheric structures.

- *Spectrum lines*

The He I spectrum line at 10830 Å provides the best magnetic field diagnostic by joint action of the Hanle and Zeeman effect with less affected by atmospheric stratification in the photosphere and lower chromosphere. The Ca II line at 8542 Å is the second prioritized one for magnetic field diagnostics because it has good sensitivity to the Zeeman effect in a wide range of magnetic scenarios. Simultaneous observations of a companion line, He I D3 at 5876 Å for He I 10830 Å and Ca II at 8498 Å for Ca II 8542 Å, are optional to help robustness of diagnostics. Simultaneous polarimetric measurements of a photospheric line are also important for identifying energy sources in the photosphere. There are photospheric lines available near the chromospheric lines, Fe I 8538 Å in the Ca II 8542 Å window and Si I 10827 Å in the He I 10830 Å window.

Mg II h and k lines at around 2800 Å are the best line to capture temperatures and velocities of fibril structures in the upper chromosphere because of higher opacity than Ca II lines. Because the lines are not accessible in a ground-based observation, they can be powerful tools for the diagnostics of the high atmosphere with SUVIT. See 2.3 for more details on selection of the spectral lines.

- *Temporal resolution*

We've realized ubiquitous occurrence of plasma ejection (i.e. jets) in the chromosphere and MHD waves pervading there. It is critical to resolve transit of jets and waves along and across the chromospheric structures (Fig. 2.2). The time scale of the dynamic phenomena regulated by magnetic fields is typically scaled with Alfven transit time, and is shorter than a few seconds when the Alfven velocity is 100 km/s and the spatial scale of 200 km (corresponding to 0.3 arcsec). In order to collect plenty number of photons required for the polarimetric sensitivity of 10^{-4}, we may have to mitigate the temporal sampling while keeping resolution of 20 sec (spatial scale of 200 km divided by the sound speed of 10 km/s) required to dissolve the acoustic travel time across the elemental structures.

- *Field-of-view*

When we use a 4K x 4K format with 0.05" sampling (critical sampling for the 0.1" resolution) on a detector, a field-of-view (FOV) becomes 200" x 200", which compromise most of medium-sized active regions. In force-free extrapolation of coronal magnetic fields, the FOV provides good coverage to reconstruct complex magnetic configuration at the core of a flare-productive active region though it is not enough to cover entire magnetic connectivity around the active region.

Simultaneous areal coverage in spectroscopy is also desired to track rapid chromospheric dynamics. This can be achieved by utilizing a filtergraph observation simultaneous with the spectrograph requiring slit scanning across the FOV. When the duration of the plasma ejection is 3 minutes with a velocity of 100 km/s, the plasma travels 30,000 km corresponding to 40 arcsec, which is the minimum requirement of the FOV to the narrow-band fieltergraph for imaging-spectroscopic observations.

- *Spectral resolution*

In the detailed spectro-polarimetric observation of the chromospheric lines, the minimum spectral resolution required to resolve a thermal widths of chromospheric lines is $\lambda/\Delta\lambda > 100{,}000$ corresponding to 3 km/s in a Doppler shift. In order to observe spectrum lines emanated from the photosphere, $\lambda/\Delta\lambda > 200{,}000$ corresponding to a Doppler shift of 1.5km/s is required.

2.3. Spectral lines compilation

The main properties of candidate chromospheric lines to be observed with SUVIT can be found in Table 2.1. The compilation includes spectral lines in the near-UV, visible, and near-infrared wavelength range. Several criteria have been taken into account to make the line list: they have to be formed within the chromosphere to allow the diagnosis of low β plasma; the lines should show enough sensitivity to plasma temperatures, velocities, and magnetic field vectors; and the line profiles should be interpreted through radiative transfer calculations.

Table 2.1. Candidates of chromospheric lines for SOLAR-C.

Spectral line	1.2λ/D [arcsec]	Photon budget [/Dl/0.1"□/sec]		Response height [km]		Zeeman effect			Hanle effect
		Continuum	Center	Te	V	geff	Blong [G]	Btrans [G]	
Mg II k 2796 Å	0.046	$2.5x10^4$	$2.6x10^5$	~1300	~1400	1.17	85	2100	X
Mg II h 2803 Å	0.046	$2.8x10^4$	$2.2x10^5$	~1200	~1300	1.33	73	1800	-
Ca II K 3933 Å	0.065	$5.5x10^5$	$2.9x10^5$	~1000	~1200	1.17	62	1500	X
Ca II H 3968 Å	0.065	$6.4x10^5$	$3.0x10^5$	~900	~1100	1.33	51	1200	-
H I β 4861 Å	0.080	$1.1x10^7$	$1.8x10^6$	~1500	~1000	1.00	16	1200	X
Mg I b3 5167 Å	0.085	$1.3x10^7$	$1.3x10^6$	~500	~600	2.00	3.7	220	X
Mg I b2 5172 Å	0.085	$1.3x10^7$	$1.0x10^6$	~500	~600	1.75	6.5	250	X
Mg I b1 5183 Å	0.086	$1.3x10^7$	$9.2x10^5$	~500	~600	1.25	9.6	360	X
Na I D2 5890 Å	0.097	$1.5x10^7$	$7.2x10^5$	~400	~600	1.17	4.7	290	X
Na I D1 5896 Å	0.097	$1.5x10^7$	$8.4x10^5$	~400	~500	1.33	3.4	230	-
H I α 6563 Å	0.108	$1.5x10^7$	$2.8x10^6$	~1500	~1300	1.00	9.7	680	X
Ca II 8498 Å	0.140	$1.1x10^7$	$3.3x10^6$	~700	~1000	1.07	6.3	300	X
Ca II 8542 Å	0.141	$1.1x10^7$	$2.1x10^6$	~800	~1200	1.10	6.7	340	X
Ca II 8662 Å	0.143	$1.1x10^7$	$2.1x10^6$	~700	~1100	0.83	8.4	430	X
He I 10830 Å (QS)	0.179	$1.8x10^7$	$1.7x10^7$	~1800	~1800	1.42	18	380	X
He I 10830 Å (AR)	0.179	$1.8x10^7$	$1.5x10^7$	~1800	~1800	1.42	9.3	270	X

The list contains the following information (from left to right):

1) Element and central wavelength (λ) of the transition. QS and AR stand for quiet sun and active region scenarios for the He I 10830 Å line.
2) Spatial resolution for each spectral line at the diffraction limit of a telescope of D=1.5m.
3) Photon budget estimation based upon the preliminary design of Solar-C instrument:
- The telescope consists of 5 mirrors coated with Al+MgF2.
- Spectrograph efficiency of 0.2.
- Detector efficiency of 0.5 at λ<300nm, 0.8 at λ>900nm, and typical CCD 300nm<λ<900nm.
- Spectral resolution of $\lambda/\Delta\lambda=2x10^5$ (corresponding to 1.5km/s), with Δλ the wavelength sampling.
- Spatial sampling of 0.1" per pixel.
- Temporal sampling of 1sec.

4) Geometrical height at which the sensitivity (response) of the spectral line core to temperature and velocity perturbations is dominant. The heights were calculated using the centroid of the corresponding response functions in the FALC atmospheric model (Uitenbroek 2006).
5) Sensitivity limit (1σ) to magnetic fields through the Zeeman effect. The quantities Blong and Btrans stand for the longitudinal and transverse component of the field vector detectable with the sampling shown above (/Dl/0.1"□/sec) and geff is the effective Landé factor.
6) The check boxes indicate that the spectral line is sensitive to magnetic fields through the Hanle effect.

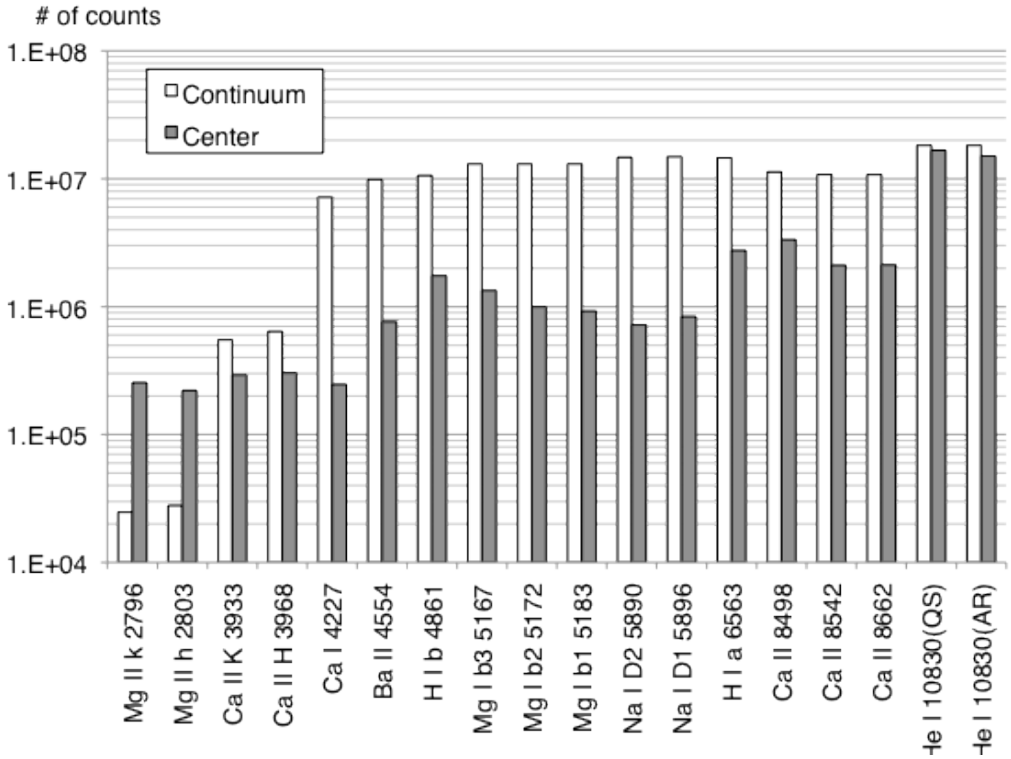

Fig. 2.4. Expected photon budged to be achieved with the 1.5mφ telescope at major chromospheric lines. See Table 2.1 for details.

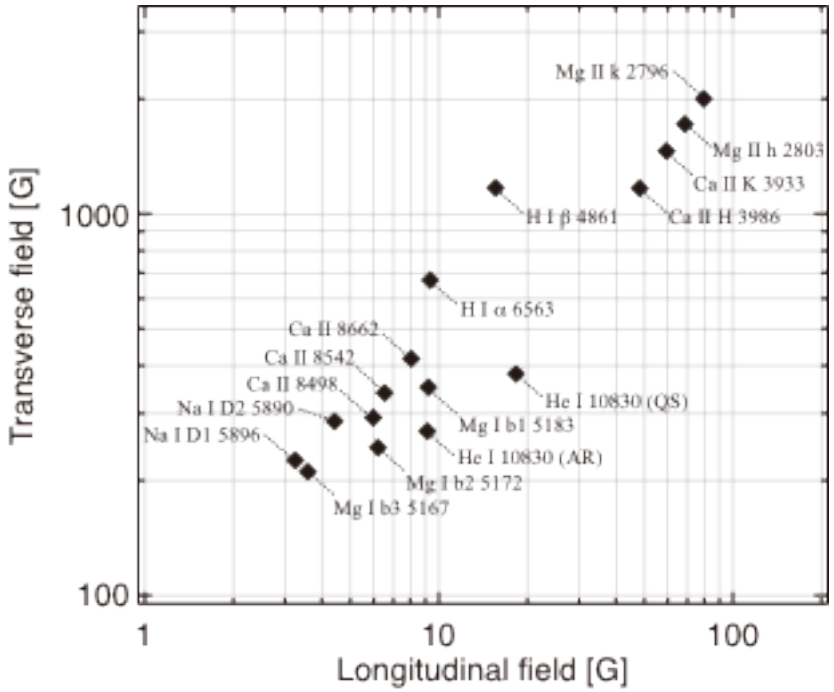

Fig. 2.5. Sensitivity of the spectral lines listed in Table 2.1 to magnetic fields through the Zeeman effect. The lower field strength means higher sensitivity.

2.3.1. Spectral lines for diagnostics of chromospheric magnetic fields

The sensitivity limit for magnetic field diagnosis through the Zeeman effect can be found in Table 2.1 and Fig. 2.5. The Na I D and Mg I b lines show good sensitivity to magnetic fields through the Zeeman effect. However, these two lines are formed low in the solar atmosphere (400 - 600 km). Therefore, they are not appropriate to diagnose the magnetic properties of the true chromospheric plasma. By contrast, the Mg II k/h and Ca II K/H lines form high in the chromosphere but their sensitivity to magnetic fields through the Zeeman effect is limited because of the short wavelengths.

The He I 10830 Å line has good sensitivity to the Zeeman effect in both, active and quiet Sun regions, although the sensitivity tends to diminish in the quiet Sun because the residual intensity decreases, i.e., the spectral line shape becomes shallow. In addition, the interpretation of the He I 10830 Å triplet is relatively easy because it is formed within a thin slab in the atmosphere. Hence, the line formation is less affected by the thermal stratification of the photosphere and lower chromosphere. Moreover, the He I 10830 Å triplet can be used for Hanle effect diagnostics. Recently, theoretical tools to model the joint action of the Zeeman and Hanle effect in the He I 10830 Å triplet have been developed satisfactorily, such that it is very powerful for magnetic field diagnostics of chromospheric and coronal structures (e.g., forward modeling and inversion code HAZEL developed by Asensio Ramos, Trujillo Bueno & Landi Degl'Innocenti 2008, see Appendix A.3.2). The longitudinal Zeeman effect at the He I 10830 Å line has a sensitivity down to 10 to 20 gauss with 0.1" spatial sampling and one second integration. We can measure transverse fields down to 0.1-100 gauss through the Hanle effect when we perform deep integration (e.g. 0.2" spatial sampling and 20 sec integration).

Table 2.2. Sensitivities (1σ) to magnetic fields at He I 10830 Å and Ca II 8542 Å.

		0.1 arcsec sampling 1 sec integration	0.2 arcsec sampling 20 sec integration
He I 10830 Å (QS)	Blong	~20 gauss	~2 gauss
	Btrans	~380 gauss (Zeeman)	~130 gauss (Zeeman) 0.1 – 100 gauss (Hanle)
He I 10830 Å (AR)	Blong	~10 gauss	~1 gauss
	Btrans	~270 gauss (Zeeman)	~90 gauss (Zeeman) 0.1 – 100 gauss (Hanle)
Ca II 8542 Å	Blong	~7 gauss	~0.8 gauss
	Btrans	~340 gauss (Zeeman)	~ 110 gauss (Zeeman)

(*) Here we assume the same instrument throughput and wavelength sampling used in Table 2.1.

The Ca II infrared triplet at about 850 nm is the second prioritized line for magnetic field diagnostics in the SUVIT on SOLAR-C. It shows good magnetic sensitivity in a wide range of magnetic scenarios, including quiet regions, which potentially remedies the weakness of the He I 10830 Å line. The longitudinal Zeeman effect especially has a good sensitivity at the Ca II 8542 Å line, and we can measure magnetic fields weaker than 10 gauss with 0.1" spatial sampling and one second integration. Of especial interest is that through the Hanle effect the linear polarization of this line is sensitive to the orientation of the magnetic field in the upper chromosphere of the quiet Sun (Manso

Sainz and Trujillo Bueno 2010) though the polarization amplitude due to the Hanle effect is relatively small (order of 10^{-4}).

In Table 2.2 are summarized the sensitivities of the spectrum lines above mentioned to magnetic fields through the Zeeman and Hanle effects.

2.3.2. Spectral lines for diagnostics of chromospheric dynamics

The chromosphere is pervaded by fast moving plasma structures. The measure of the dynamic properties of such structures requires not only spectral lines with great sensitivity to temperature variations at certain wavelengths but also short integration times. Since such observations are done typically with filter instruments with limited spectral bandwidths little contamination from nearby wavelengths is also desired. In this sense, the Mg II k/h spectral lines at around 2800 Å are suitable for the SUVIT in SOLAR-C. Their sensitivity to temperature variations is great in the upper chrmosphere because the opacity of these lines is very large at the line core. High temperature sensitivity lines also allow investigating heating processes in the chromosphere. Although the low photon budget at the spectral range of the Mg II lines is a limiting factor for the polarimetric measurement (Table 2.1 and Fig. 2.4), it is well enough to do high cadence spectroscopic observation (without polarimetry) with exposure times shorter than 0.1 sec.

Other spectral lines like the Ca II infrared triplet at about 850 nm and Ca II H and K lines are good candidates for tracking the dynamics of the various chromospheric events, by analyzing observed line profiles along with cloud modeling and/or forward modeling of the lines obtained from numerical simulation of the chromosphere (see Appendix A.3.1 and A.4).

2.4. Configuration of the instrument

A basic concept of the optical design of SUVIT on SOLAR-C is to use a similar configuration with the Solar Optical Telescope (SOT) on HINODE, which allows us to make use of the technical heritage that the Japanese solar physics group developed in HINODE/SOT (Tsuneta et al. 2008, Suematsu et al. 2008). A major difference is to expand the diameter of the aperture from 0.5 m to 1.5 m, which is aiming to collect one order of magnitude more photons than HINODE/SOT as well as angular resolution better than 0.1 arcsec. This is essential to achieve the high polarimetric sensitivity for chromospheric diagnostics. SUVIT consists of the telescope and focal plane instruments. The focal plane instruments are installed into two packages:

1) Spectrograph package
   It consists of an Echelle grating spectrograph for spectro-polarimetric observations and a correlation tracker for the image stabilization system.

2) Imager package
   It consists of a broadband filtergraph utilizing interference filters for monochromatic imaging observations and a narrowband filtergraph utilizing a tunable narrowband filter for imaging spectrograph allowing to make Dopplergrams and magnetograms.

The combination of the multiple instruments enables to cover wide variety of scientific targets. The optical block diagram of the instruments is shown in Fig. 2.6. The telescope collects incident lights and feeds into the focal plane packages. The tip-tilt mirror in the telescope is driven to remove attitude jitter of the spacecraft using signals of image displacements detected with the correlation tracker in the spectrograph package. Polarization modulators are to be installed in each focal plane package while polarization calibrator is possibly implemented in the telescope. Preliminary parameters of pixel scales and typical exposures are summarized in Table 2.3. Table 2.4 shows possible choices of the spectrum lines at each focal plane instrument. The combination of the spectrum lines provides the spectrum diagnostics completely covering from the photosphere through the middle to the upper chromosphere.

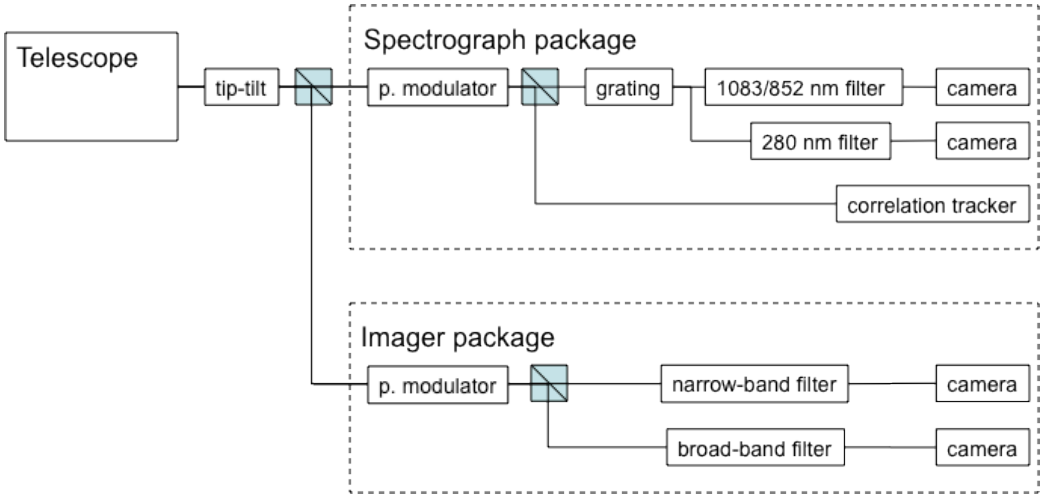

Fig. 2.6. Optical block diagram of the focal plane instruments.

Table 2.3. Configuration of the focal plane instruments.

	FOV	Pix scale	Exp.	Note
Correlation tracker (CT)	10”x10”	0.2”	< $2x10^{-3}$ sec	faster readout than 5kHz. 50x50 format
Spectro-polarimeter (SP)	184”×184”	0.09”	~1 sec	2 pix sampling of 0.18”res 2K pix along slit, S/N~10^3.
		0.18”	>10 sec	2x2 pix binning to reach S/N~10^4.
Broadband filtergraph (BF)	164”×164”	0.04”	<0.1 sec	2.5 pix sampling of 0.1” res 4K×4K detector
Narrowband filtergraph (NF)	205”×205”(1) 120”x120”(2)	0.05”	<1 sec	2 pix sampling of 0.1” res 4K×4K or 2Kx2K detector

(1) The optical configuration allows us to cover the FOV of 200” x 200” if a tunable filter has an aperture big enough to cover the FOV.

(2) The 120” x 120” FOV is available when the diameter of a Lyot filter-type tunable filter has a diamete of 50 mm at the F/40 telecentric focus. In order to accommodate larger FOV coverage in the NF, we need optics to convert magnification in the channel.

Table 2.4: Spectrum lines to be observed in SUVIT on SOLAR-C.

Spectrum lines		SP	BF	NF	Purpose
Mg II k	279 nm	x	x		T and V in the chromosphere
Continuum	TBD		x		Imaging and T in the photosphere
CN band	388 nm		x		Magnetic elements in the photosphere
Ca II K	393 nm		x		Structures in the chromosphere
Mg I b	517 nm			x	V and B in the low chromosphere
Na I D	589 nm			x	V and B in the low chromosphere
Fe I	525 nm or 630 nm			x	V and B in the photosphere
H I α	656 nm			x	Structures in the chromosphere
Ca II	854 nm	x		x	T, V, and B in the chromosphere
He I	1083 nm	x			V and B in the chromosphere

2.5. Optical telescope assembly

2.5.1. Optical design

The optical telescope assembly (OTA) of SUVIT employs the following basic characteristics in the baseline design for exploring its technical feasibilities:

- Aplanatic Gregorian 2 mirror telescope.
- Entrance aperture with the 1.5mφ diameter.
- Heat rejection mirror at the primary focus.
- Axial symmetric optics to give negligible instrumental polarization.
- Afocal interface between the telescope and the focal plane instruments.

The aperture size of the telescope is the most critical item in the concept of the telescope, which is driven by the scientific requirements. We are going to optimize the aperture size down to 1m according to future investigation of technical and scientific feasibilities. Another factor to design the telescope is a limitation of the length of the telescope to fit within a fairing of the launcher (JAXA H-IIA rocket). Based on a study of positional tolerance of the secondary mirror, the distance between the primary mirror (M1) and the secondary (M2) is decided to be 2.8 m as a baseline design. Basic parameters of the optical design of the telescope are summarized in Table 2.5, and its overall configuration is shown in Fig. 2.7. The afocal interface has an advantage to relax the positional tolerance between the telescope and the focal plane instruments. Because the wider wavelength coverage (280 nm to 1.1 μm) than Hinode is required in SUVIT-OTA, the refractive optical design to make a collimated beam in HINODE/SOT is not appropriate. Instead, we are going to realize it using a collimator mirror unit (CMU), which consists of three off-axis aspheric mirrors. The third mirror of the CMU can be used as a tip-tilt mirror for the image stabilization system. Optical performance of the telescope is shown in Fig. 2.8 as is evaluated with spot diagrams at the image plane focused with an ideal lens located at the exit pupil. The RMS spot radius is well within the spot size due to diffraction within the field of 200 arcsec.

There are two field stops in the telescope. One is a heat dump mirror (HDM) at the

focus of M1, which is 45-deg flat mirror with a central hole passing the beam of field of view of 300 arcsec (TBD), and to reflect the unnecessary solar illumination outside of the hole from the side of the telescope. The other is a secondary field stop (2FS) at the Gregorian focus, which is again to reflect the unnecessary solar illumination out of the field of 220x220 arcsec (TBD), which a bit oversizes the area of detectors in the focal plane instruments.

Table 2.5. Basic optical parameters of SUVIT-OTA.

		SOT-OTA (HINODE)	SUVIT-OTA (SOLAR-C)
Entrance pupil (mm)		500	1500
M1 – M2 distance (mm)		1500	2800
M1	outer diameter (mm)	560	1580
	clear aperture (mm)	509	1513
	curv. radius (focal) (mm)	2339.4 (1169.7)	4629.34 (2314.67)
	conic const.	-0.9706	-0.990927
M2	outer diameter (mm)	159	340
	clear aperture (mm)	147	320.5
	curv. radius (focal) (mm)	524.94 (262.47)	835.494 (417.747)
	conic const. (mm)	-0.3996	-0.54815
HDM outer radius (mm)		32.83	43.1
Eff. f-length at 2nd focus (mm)		4527 (F/9.05)	14300 (F/9.54)
CMU focal length (mm)		271	572
Exit pupil diameter (mm)		30	60

(note: The unit is in mm.)

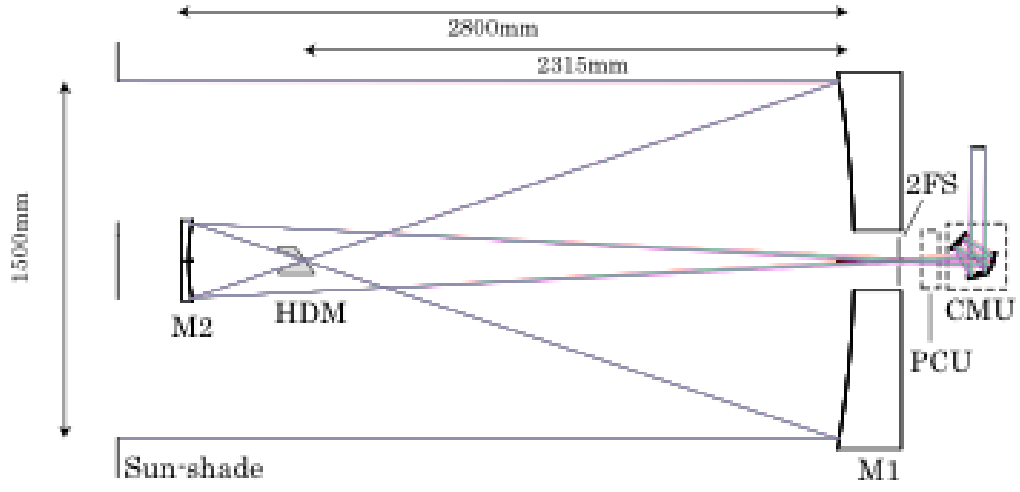

Fig. 2.7. The optical configuration of the telescope assembly of SUVIT. A polarization calibration unit (PCU) can be inserted after the Gregorian focus for calibrating polarization responses of the focal plane instruments.

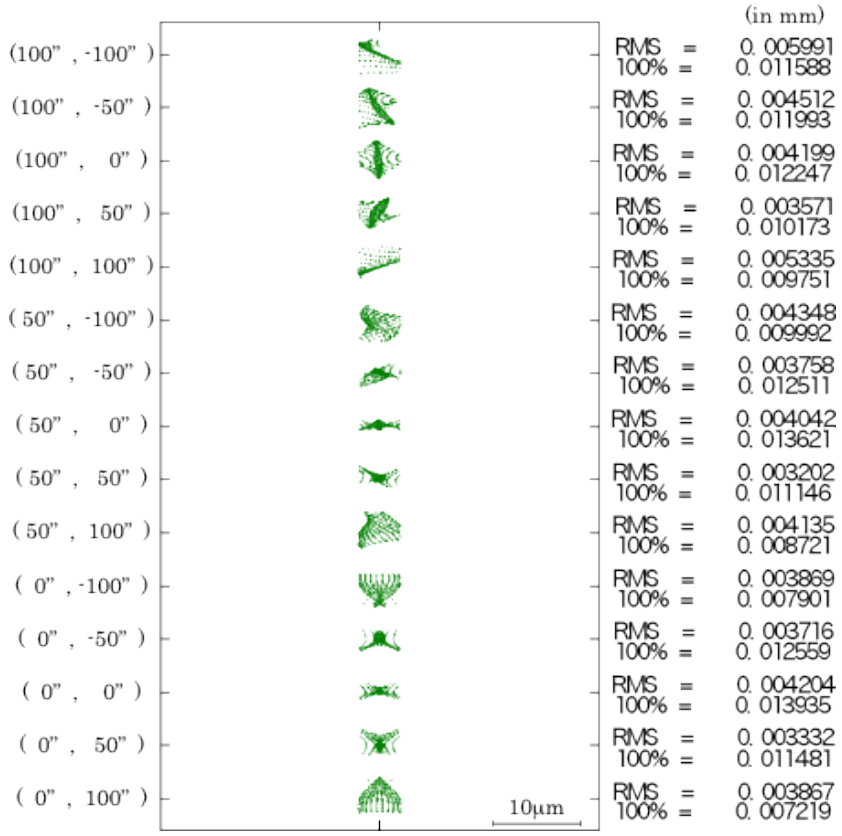

Fig. 2.8. Spot diagrams of the telescope evaluated at the image plane focused with the ideal lens located at the exit pupil. Note that the RMS spot radius due to diffraction is about 6 μm at 500 nm.

2.5.2. Mirror coating and photon budgets

In order to observe the spectrum lines prioritized based on the scientific point of view, it is essential to cover the wavelength range from 280 nm to 1.1μm. A coating design of the mirrors is critical not only to have higher throughputs for precise polarimetric measurements but also to minimize absorption of the solar illumination at the mirrors of the telescope. The silver-based reflective coating used in HINODE/SOT has high reflectivity in the visible and NIR wavelength range. But its reflectivity is very low in the UV wavelengths shorter than 350 nm. Aluminum coating is good alternative in UV although its reflectivity is slightly lower in visible and NIR (Fig. 2.9).

When we apply the aluminum coating to the mirrors in SUVIT-OTA, and if we assume efficiencies of the focal plane instruments, we can estimate the number of photons to be collected by the telescope per a resolution element and per unit time. Fig. 2.10 shows effective areas and efficiencies as a function of the wavelength, in which we assume that the spectrograph or filtergraph efficiency is 0.2, the quantum efficiency of the detector is 0.8 at λ>900nm, 0.5 at λ<300nm, and typical QE of CCD at 300nm<λ<900nm. The instrument has a total efficiency of about 0.1 in the observing wavelength range even when we use the aluminum coating, and the effective area is expected to be 1000 to 2500 cm^2 dependent on the wavelength. Fig. 2.11 shows the number of photons to be achieved with the telescope at major chromospheric lines

where we assume wavelength sampling of $\lambda/\Delta\lambda=2x10^5$, spatial sampling of 0.1" /pixel, and temporal sampling of 1 sec. The polarimetric diagnostics of chromospheric lines require the polarimetric sensitivity of 10^{-4}. This means that we have to collect 10^8 photons in a resolution element if the sensitivity is limited by a photon noise. The figure indicates that we can collect more than 10^6 photons at the line center of each spectrum line with the sampling mentioned above. It appears that we can collect 10^8 photons at the line center of He I 10830 Å and Ca II 8542 Å if we apply 2x2 pixel summing (i.e. 0.2" per pixel) and integrate for 10 to 20 seconds, that is short enough to temporally resolve the dynamics in the chromosphere.

As is shown above, the 1.5mφ aperture and the aluminum coating provides a good photon budget satisfying the scientific requirements at observing spectrum lines. For further improvements of the throughput and for helping a thermal design by minimizing the heat absorption at the mirrors of the telescope (see 2.5.4), it is desirable to develop a mirror coating with higher reflectivity in visible and NIR while keeping the reflectivity at 280 nm.

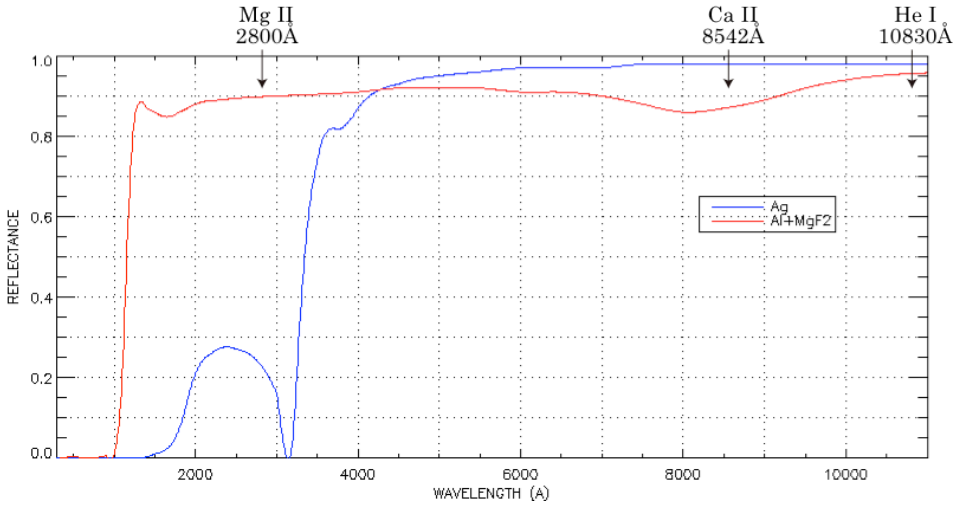

Fig. 2.9. Mirror reflectivities of the silver (Ag) coating and the aluminum (Al) coating with MgF2 over-coating.

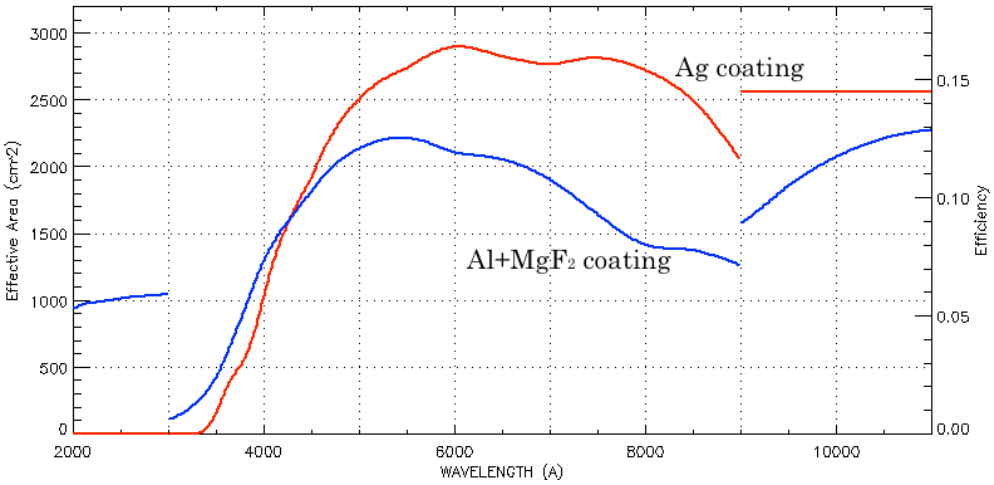

Fig. 2.10. Effective area of the SUVIT with the 1.5 mφ aperture. The telescope consists of 5 mirrors with Ag coating (red line) and Al + MgF2 coating (blue line).

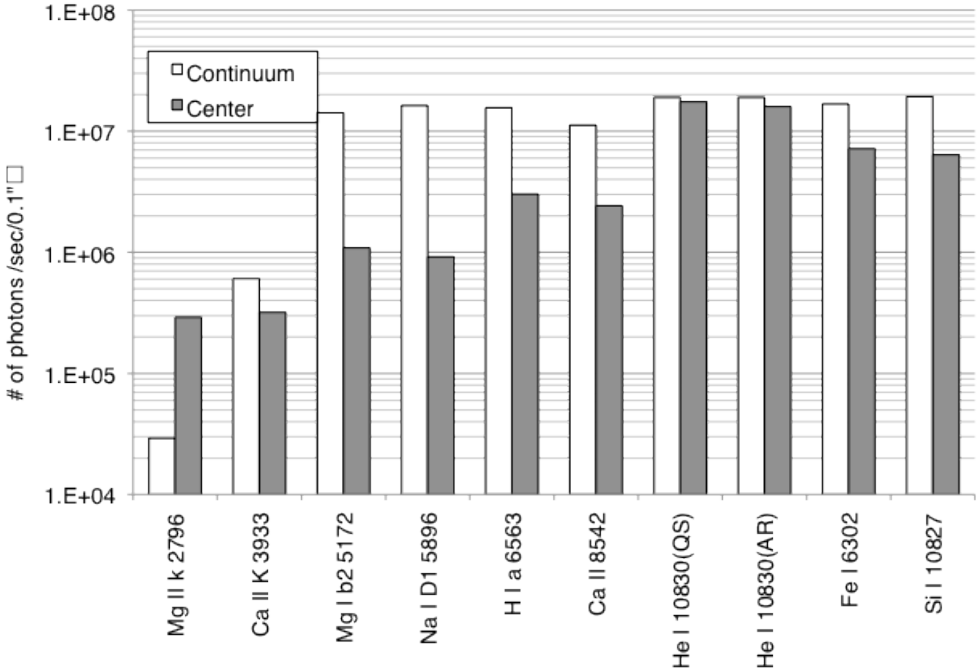

Fig. 2.11. The number of photons to be achieved with the telescope at observing chromospheric and photospheric lines. The gray bars represent the number of photons at the line core of each spectrum line while the white bars are at nearby continuums.

2.5.3. Structure design

The structural design of the SUVIT-OTA basically follows that of Hinode SOT. M1 and M2 for the aplanatic Gregorian are made of light-weighted low expansion material of either ULE or Zerodur. The light-weighting technology of telescope mirrors has been much advanced since Hinode OTA manufacturing era. We expect 90 % mass reduction with an open back mirror structure. Then the M1 of 1.5 m aperture would weigh less than 150 kg. The light-weighted mirrors are crucial not only from tight weight budget of satellite but also from ground testing of telescope optical performance because of small gravitational mirror deformation. The surface figures of the mirrors are ellipsoids as conic constants shown in Table 2.5. Since null correctors for these

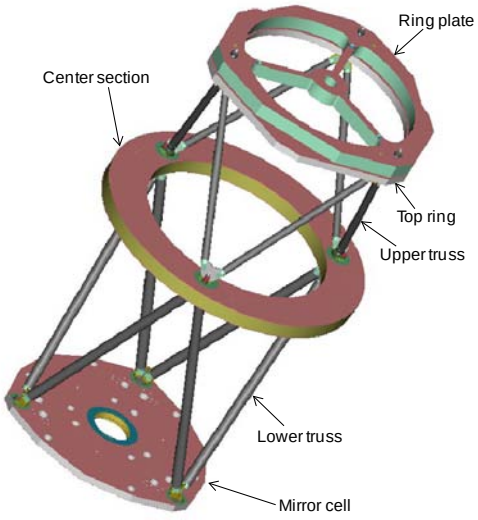

Fig. 2.12. CFRP truss structure of SOT-OTA in HINODE.

aspheric mirrors can contribute to inaccurate surface figures, we should include a M1-M2 combination test in the mirror polishing process. We note that flight-model supporting mechanism for M1 also should be used in the combination test so that the surface error due to the mounting can be corrected in the polishing process. The HDM and the 2FS at the primary and the Gregorian focus are to be made of aluminum alloy and to be coated with a silver coating.

The short Gregorian telescope demands small static mis-alignment tolerances for M1 and M2, on the order of a few tens microns for decenter and despace or several arcsec for tilt, and a micron-order de-space short-term stability on-orbit during observations (Table 2.6). To meet this tolerance, the telescope structure is made of a truss of ultra-low-expansion CFRP (Carbon Fiber Reinforced Plastics) pipes in a Graphite Cyanate matrix, whose CTE is proven to be smaller than 0.1 ppm/K, and the dimensional change due to moisture absorption is about 30 ppm, which is much smaller than conventional epoxy matrix composite pipes (Fig. 2.12). CFRP honeycomb sandwich panels are adhesively bonded with upper and lower truss pipes without any metal junctions to save weight and also to avoid differential CTE, which may cause unexpected thermal distortion.

Table 2.6. Mis-alignment sensitivity of SUVIT-OTA as contrasted with Hinode OTA.

Component		Aberration	SUVIT-OTA[1)] (SOLAR-C)	SOT-OTA[1)] (HINODE)
M1	Despace	Defocus	3.4 μm	8.3 μm
		Spherical	500 μm	2750 μm
	Decenter	Coma	48.5 μm[2)]	165 μm
	Tilt	Coma	4.3 arcsec[3)]	28.8 arcsec
M2	Despace	Defocus	3.3 μm	7.6 μm
		Spherical	500 μm	2800 μm
	Decenter	Coma	48.5 μm[4)]	165 μm
	Tilt	Coma	21 arcsec	111 arcsec

1) The positional and angular sensitivities to the mis-alignment of M1 and M2 are evaluated in the condition that a Strehl ratio is reduced to 0.8 from 1.0 at 633 nm (He-Ne laser) at the field center.
2) The coma aberration can be compensated by M2 tilt of 0.189°.
3) The coma aberration can be compensated by M2 tilt of 0.168°.
4) The coma aberration can be compensated by M2 tilt of 0.20°.

Mounting of M1 is one of the most critical parts in SUVIT-OTA. The primary mirror is supported by three stress-free mounting mechanisms seated on the CFRP bottom panel, interfaced with three superinvar pads bonded on the side of the mirror (Fig. 2.13). The pad interface of the mounting mechanism provides a kinematic mount for M1. The pad interface thus avoids stresses to the mirror resulting from dimensional errors in machining or temperature change. In order to make it sure, the mounting mechanisms are to be used in the wavefront error measurements of M1 and M2 as noted above. The only significant surface error of the primary mirror is caused by the difference of CTE between the superinvar pads and the ULE, which constrains the best-performance temperature range of the primary mirror to be between -15 to 55℃(TBD).

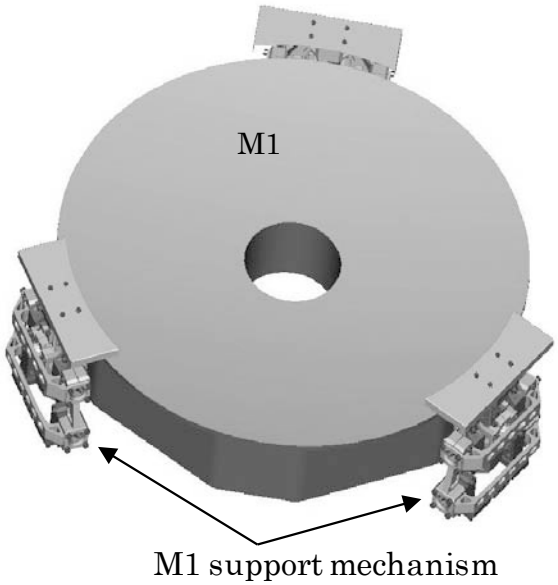

Fig. 2.13. Hinode OTA M1 and its supporting mechanism.

M2 is supported by a superinvar tripod-shaped pad of stress relief spring legs that are glued at the backside of M2. The surface error of the secondary mirror can be again caused by the CTE difference between the superinvar pad and the ULE, and it constrains the best-performance temperature range between 0 to 40℃(TBD). Since the positional tolerance of M2 is tighter than that of Hinode OTA, it is demanded to have in-flight alignment mechanism of M2 by occasional commanding from the ground. As shown in Table 2.6, the positional tolerances of M1 and M2 are much relaxed if M2 tilt adjustments are possible. We expect the mis-alignment of M2 does not occur frequently but does in post-launch and seasonal intervals. The amount of M2 tilt mis-alignment can be derived by analyzing a coma aberration of a wavefront error using a phase diversity method in one of the focal plane instruments.

2.5.4. Thermal design

Solar illumination of about 2 kW is inevitably impinged onto the primary mirror at the bottom of the SUVIT-OTA during solar observations from its aperture. It is critically important to make a thermal design to dump such a large heat load to space and maintain optical and structure components within allowable temperature ranges with small temperature fluctuation. In order to identify technical difficulties in the thermal design of the 1.5mφ telescope, we investigate thermal environment of the telescope using a scaled-up thermal model (Fig. 2.15) of Hinode SOT-OTA except higher solar absorption coefficient α of M1 and M2 with taking into account the lower reflectivity of the aluminum coating (α ~ 0.1 for Al coating while α ~ 0.05 for Ag coating at begin-of-life (BOL), see Table 2.7). The thermal design concept of Hinode SOT-OTA is summarized as follows:

1) Most of the incident energy is reflected back by M1 and dumped out to space by the

HDM through the heat dump window on the side of the telescope.

2) The sunshade has an optical solar reflector facing the Sun to keep it cold, while the upper area of the shield tube is used as a radiator.
3) The solar heat absorbed in M1 is radiatively transmitted to a telescope lower tube from its side and from a bottom cooling plate just beneath M1.
4) The solar heat absorbed by M2 is radiatively transmitted to the radiator from its backside.
5) The heat absorbed by the 2FS and CMU is conductively transferred to a mirror cell and also emitted out through their housings, and is finally radiatively transmitted to the lower tube.

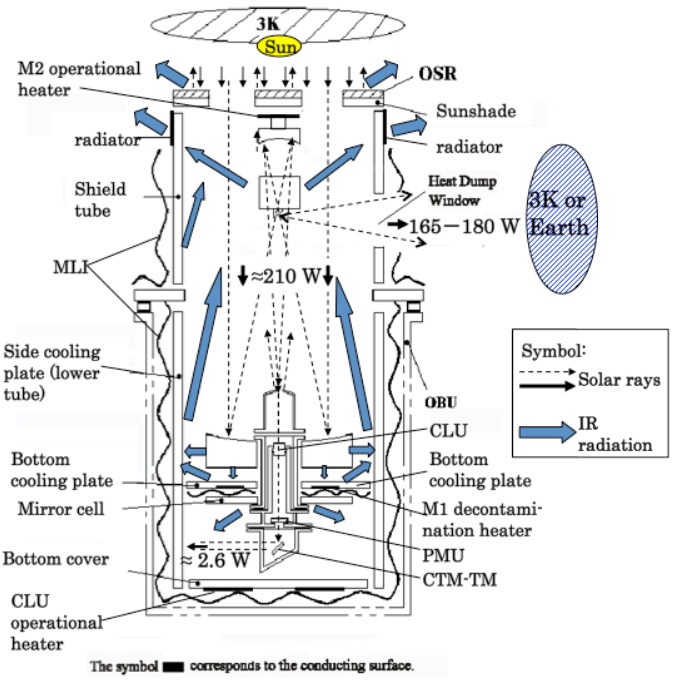

Fig. 2.14. Thermal design concept in the Hinode OTA.

6) The heat absorbed by the HDM is conductively transferred to the cylindrical structure supporting the HDM and outer spiders, and then radiatively transferred to the radiator on the shield tube and space through the heat dump window.
7) The heat of the lower tube and the shield tube is radiatively emitted directly to the space through the entrance aperture and indirectly via the radiator of the sunshade and upper shield tube.
8) The OTA is thermally insulated from the spacecraft. The OTA is physically connected to an optical bench unit (OBU) only by mounting legs of low-thermally conductive titanium and is radiatively de-coupled from the OBU.

Table 2.7. Solar light absorption coefficient and absorbed energy at begin-of-life (BOL).

Components	Absorption coeff. α	Incident radiation (W)	Absorbed radiation (W)
M1	0.12	2074.9	244.8
HDM	0.1	1830.1	175.4
M2	0.12	76.2	9.0
CMU	0.11	19.4	2.1
Total	---	----	431.4

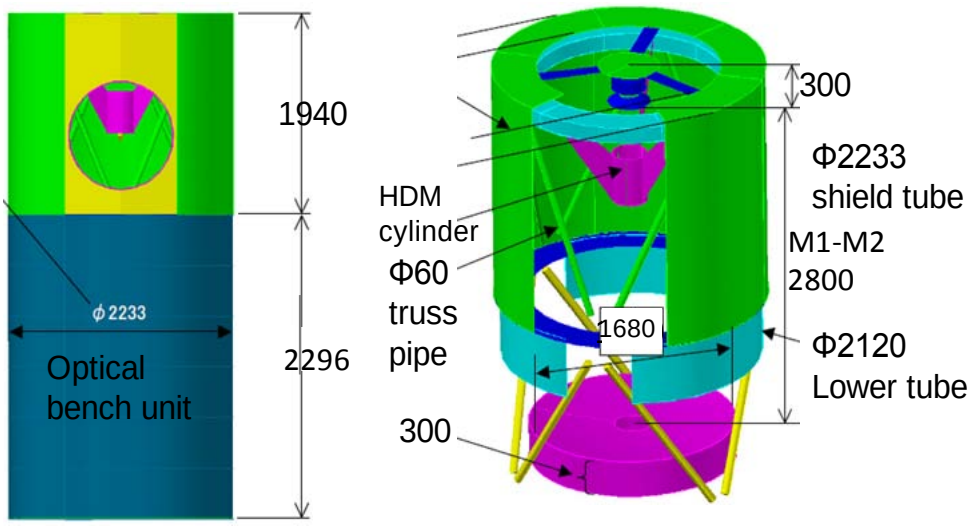

Fig. 2.15. Thermal math model for SUVIT-OTA.

Predicted temperatures of optical components at BOL are given in Table 2.8, where the orbit of the spacecraft is either the sun synchronous polar orbit (SSO) or the geo-synchronous orbit (GEO). The base model is simply a scaled-up model of Hinode SOT-OTA, and we find that it gives unacceptably high temperatures both for the primary mirror and HDM, especially in the case of SSO. When we increase the area of the radiator on the shield tube (Mod-1) and increase the conductivity between HDM and the HDM cylinder and increase the area of the HDM cylinder (Mod-2), it is possible to make the temperatures marginally within the acceptable range even in the case of SSO.

Table 2.8. Predicted temperatures of the components at BOL.

Components	Base model		Mod-1	Mod-2
	SSO	GEO	SSO	SSO
M1 surface	61	49	52	52
M2 surface	-2 ~ -7	-24	-12 ~ -8	-12 ~ -7
HDM surface	109 ~ 111	100	103 ~ 104	60 ~ 61
CMU	34 ~ 37	22 ~ 24	24 ~ 27	24 ~ 26

It turned out, however, that those modifications still cannot lower the temperature of M1, especially when the solar absorption coefficient αis degraded at end-of-life (EOL) and the heat absorption at M1 increases by about 100W (Table 2.9). To lower the temperature in this case, more drastic modifications are necessary, in which an additional heat dump system from M1 (e.g. change the bottom of OBU to a radiator) is accommodated (Mod-3). The prediction based on the modification indicates that we can obtain the acceptable temperatures lower than 50 ℃ even at EOL if the heat load of about 100W at M1 is dumped at the bottom of the telescope and is transferred toward the spacecraft bus (Table 2.10). It is described in section 5.5 that there is a feasible concept for transferring the heat load from the telescope to the spacecraft bus, and for dumping it from a radiator on the side surface of the bus.

It is clear from the thermal model investigation that GEO has an advantage to have

the moderate temperatures and lower temperature fluctuation because less affected by infrared radiation from the earth. Another possible solution for lowering the temperatures is to employ a mirror coating of high reflectivity in UV and low solar heat absorption like the silver coating (see 2.5.2), which is now under investigation.

Table 2.9. Solar light absorption coefficient and absorbed energy at end-of-life (EOL).

Components	Absorption coeff. α	Incident radiation (W)	Absorbed radiation (W)
M1	0.17	2074.9	348.6
HDM	0.1	1726.3	165.4
M2	0.17	71.9	12.1
CMU	0.11	18.6	2.0
Total	---	----	528.2

Table 2.10. Predicted temperatures of the components at EOL.

Components	Base model + Mod-2		Base model + Mod-2 + Mod-3	
	SSO	GEO	SSO	GEO
M1 surface	80	70	52	39
M2 surface	0 ~ 4	-17 ~ -16	-2 ~ 3	-18 ~ -17
HDM surface	63 ~ 64	51	61 ~ 62	47 ~ 48
CMU	41	29	19	4

2.6. Focal plane instruments

2.6.1. Interface with the telescope

The collimated beam from CMU is spitted by a 50:50 beam splitter (BS) inside the OTA, and is fed into the two focal plane packages (Fig. 2.16). The afocal interface between the telescope and the focal plane instruments helps to relax the positional tolerance in the alignment of the packages. The third mirror of CMU can be used as a tip-tilt mirror (TM) of the image stabilization system, and works to remove the attitude jitter of the spacecraft in both the beams going to the two packages. The polarization calibration unit (PCU) is to be inserted between the 2FS and CMU to produce specific polarization states for polarization calibration, where the polarization modulators are installed in each focal plane packages as is shown in Fig. 2.6.

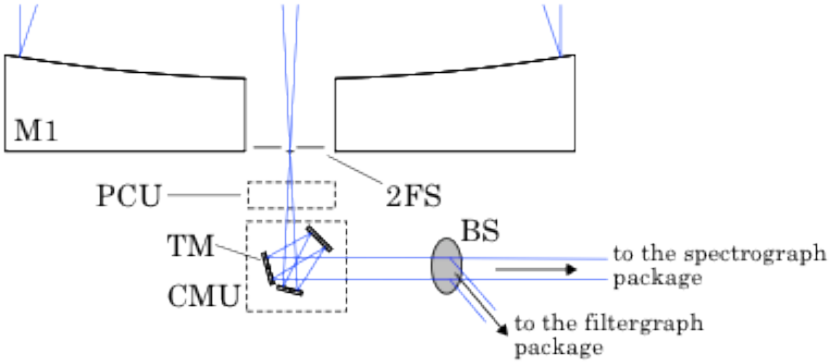

Fig. 2.16. Concept of the beam splitting inside OTA. The beam splitter is located behind the CMU, and feeds the collimated beam into the two focal plane packages.

2.6.2. Spectro-polarimeter

The spectrograph package consists of the spectro-polarimeter (SP) and the correlation tracker (CT). The SP is an instrument for obtaining full Stokes parameters of spectral line profiles, and provides precise polarimetric measurements of the chromospheric and photospheric lines to diagnose magnetic fields in the solar surface. The preliminary concept of the spectrograph is to employ a Littrow spectrograph configuration similar with the spectro-polarimeter (SP) of HINODE SOT. The optical configuration of the spectro-polarimeter is shown in Fig. 2.17 (*top*). The basic parameters are summarized in Table 2.11. It consists of an Echelle grating and an offset-aspheric mirror for collimating and reimaging the beam before and after the grating. In the current design, the spectrum bands around He I 1083 nm, Ca II 854 nm, and Mg II h/k 280 nm can be observed simultaneously in the same diffraction angle with different orders (Fig. 2.17 *bottom*). The observing bands include not only chromospheric lines but some photospheric lines in the observing wavelengths (e.g. Si I at 1082.7 nm) allowing simultaneous observation of both the photosphere and the chromosphere. Is to be switched by changing band-pass filters. Scanning over the FOV across the slit is done with a scan mirror located in front of the slit. In order to minimize scanning duration, a multi-slit configuration is considered, in which two or three slits are located with 60'' – 80'' separation to get spectra at multiple locations simultaneously (Fig. 2.17 *bottom*). A Wollaston prism is installed in front of the detector to measure the orthogonal polarization states simultaneously. In order to observe the He I line at 1083 nm, it is required to use an infrared detector instead of CCD. But infrared detectors generally require low temperatures environment to suppress noises due to dark currents. We are now investigating a possible usage of an HgCdTe detector with a 1.7 μm cut-off which can be operated with relatively higher temperatures (T~200K). The detector is also sensitive to 854 nm with a good efficiency. In order to observe Mg II h/k lines at 280 nm in SP, getting co-focus at the slit is optically difficult because the wavelength is very different from 1.1 μm and 854 nm. It is under investigation to make an optical design allowing observations at 280 nm in SP.

The precise polarimetric measurements for diagnostics of chromospheric fields require 10 – 20 sec integration at each slit position to achieve the 10^{-4} polarimetric sensitivity. In addition to the deep polarimetric observation, the instrument is to be

designed to support rapid scanning to make spectroscopic observations for study of chromospheric dynamics and a spectro-polarimetric observations for photospheric magnetic fields over the FOV with 0.1 sec – 1 sec integration at each slit position. Basic observing modes with the instrument are summarized in Table 2.12.

Table 2.11. Basic parameters of the spectrograph.

Type	Littrow spectrograph
Entrance pupil	60 mm
Focal length @ slit	1650 mm (F/27.5)
Detector size	2048 x 2048, 18μm/pixel
Pixel scale	0.09 arcsec /pixel
FOV along slit	184 arcsec
Blaze angle	63.4°
Groove	110 / mm
Slit width	TBD μm
Sampling dispersion	$\lambda/\Delta\lambda$=2.5 x10^5

Wavelength bands	1083 nm	854 nm	280 nm
Spectrum lines	He I	Ca II	Mg II
Order	15	19	58
Wavelength sampling	43 mÅ	34 mÅ	11 mÅ

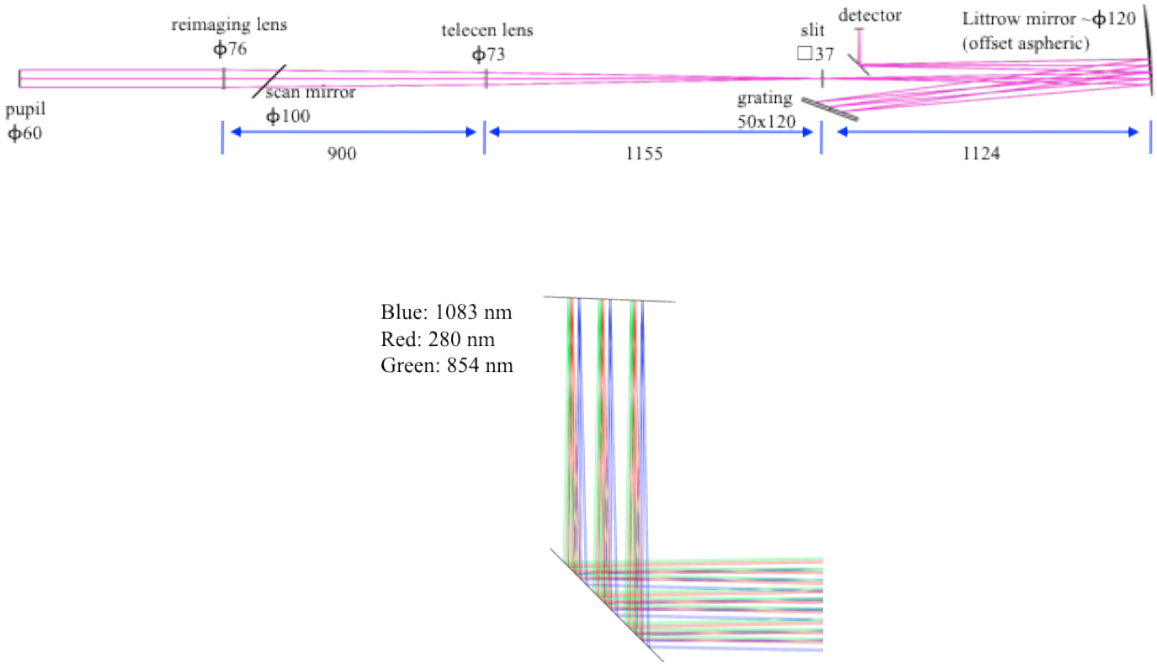

Fig. 2.17. Optical configuration of the spectro-polarimeter (*top*), which allows simultaneous observation of the three wavelength bands at around 1083 nm, 854nm, and 280 nm at the same diffraction angle (*bottom*). The figure shows optical rays at each spectral band when three slits are located at the image plane.

Table 2.12. Basic observing modes of SP in SUVIT.

Rapid mode	High-speed spectroscopic observation for studies of dynamics. − Spectral lines: Mg II h/k 280nm, Ca II 854 nm − Integration time: ~0.1 sec at each slit position. − Duration: ~2 minutes to scan 100 arcsec FOV.
Normal mode	Spectro-polarimetric observation for study of photospheric magnetic fields and chromospheric dynamics. − Spectral lines: He I 1083 nm, Si I 1082.7 nm, Ca II 854 nm − Integration time: ~1 sec at each slit position. − Duration: ~20 minutes to scan 100 arcsec FOV.
Deep mode	Spectro-polarimetric observation for study of chromospheric magnetic fields. − Spectral lines: He I 1083 nm, Si I 1082.7 nm, Ca II 854 nm − Integration time: 10 – 20 sec at each slit position. − Duration: 20 – 40 minutes to scan 10 arcsec FOV. (Sparse scanning is used to map wide FOV.)

2.6.3. Broad-band filtergraph

The purpose of the broad-band filtergraph (BF) is to get a monochromatic image of the solar photosphere and chromosphere using interference filters at the best possible spatial and temporal resolution. The optical design is very simple and is shown in Fig. 2.18, in which a filter wheel and a shutter are located in front of the detector. The basic optical parameters and candidates of the filter pass-bands are shown in Table 2.13. A key for developing the channel is to make an optical design allowing co-focus at around 280 nm and longer than 400 nm.

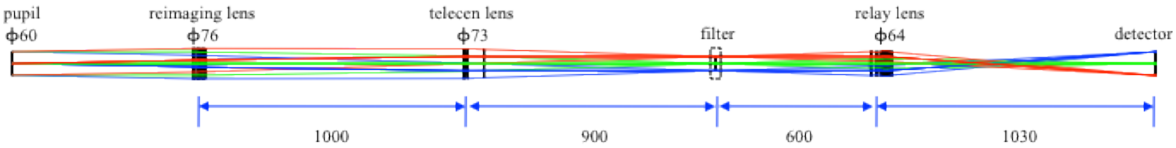

Fig. 2.18. Optical configuration of the broad-band imager.

Table 2.13. Basic parameters of the broad-band imager.

Entrance pupil	60 mm
Focal length	2475 mm (F/41.3)
Detector size	4096 x 4096, 12μm/pixel
Pixel scale	0.04 arcsec /pixel
FOV	164 arcsec x 164 arcsec

Pass-bands	279 nm	380 nm	393 nm	TBD
Spectrum lines	Mg II k/h	CN band	Ca II K	Contin.

2.6.4. Narrow-band filtergraph

The narrow-band filtergraph (NF) is an important instrument to get monochromatic imaging in chromospheric and photospheric lines, and to make Dopplergram and magnetogram observations with covering relatively wide field of view. A tunable filter (TF) is a key component in the narrowband filtergraph. There are two possible types of TF for SUVIT, (1) Lyot filter and (2) Fabry-Perot filter. The Lyot filter is a narrow-band filter using a birefringence of calcite blocks, where peak wavelengths of its transmission can be tuned with either rotating wave plates or liquid crystal variable retarders (LCVRs). There are two possible ways in the Fabry-Perot filter. One is to use two glass plates and adjust the gap between them to tune the central wavelength of the transmission (air space). The other is to use a plate made of ferroelectric crystal ($LiNbO_3$) and apply high voltages to tune the wavelength. There are advantages and disadvantages among them, which are summarized in Table 2.14, and a trade-off study is now under going.

Table 2.14. Comparison between Lyot filter and Fabry Perot filter for SUVIT.

	Lyot filter	Fabry Perot	
		Air space	$LiNbO_3$
Speed of incident beam	F ~ 40	F ~ 200	F~90
Necessary diameter D = 1.5m, FOV=2'φ D = 1.5m, FOV=3'φ	 ~36 mm ~54 mm	 ~180 mm ~270 mm	 ~81 mm ~120 mm
Transmission	~5 %	~70 %	~70 %
Simultaneous 2-pol.	impossible	possible	possible
Simultaneous multi λ	(in principle possible)	impossible	possible (y-cut)
Structure	complex	high accuracy	simple
Oil	necessary	free	free
Control device	rot. WP or LCVR	Piezo	$LiNbO_3$
Past experience	HINODE SOT	SOHO LASCO/C1	SUNRISE IMAX
Advantage	- Smaller aperture - Tolerant - Large FSR - Stable flat field	- Fast tuning - High throughput	- Light and simple - Smaller aperture (than air speace FP)
Disadvantage	- Many pol. elements - Need oil - Low throughput - Long	- Big and heavy - High precision - Unstable flat field - Small FSR	- High voltage - Slow tunig - Small FSR - Unstable flat field - Vulnerability

A possible optical design is shown in Fig. 2.19, where we use a Lyot filter as TF, and locate it in a telecentric beam of F/40 to make a uniform wavelength over the field of view. Several wavelength pass-bands can be switched by changing blocking filters located in front of TF. The reimaging lens is possibly shared with the broad-band filtergraph in the imager package. The basic parameters of the optical configuration are summarized in Table 2.15. Requirements on TF are summarized in Table 2.16. The FOV available with NF depends on how big the TF diameter can be fabricated. When the

diameter of the Lyot filter is 50 mmφ at the telecentric focus of F/40, the FOV is to be limited within 120” x 120”. In the case of the air-space Fabry-Perot filter at the telecentric focus of F/200, the FOV is to be limited within 90” x 90” when the diameter of the TF is 180 mmφ.

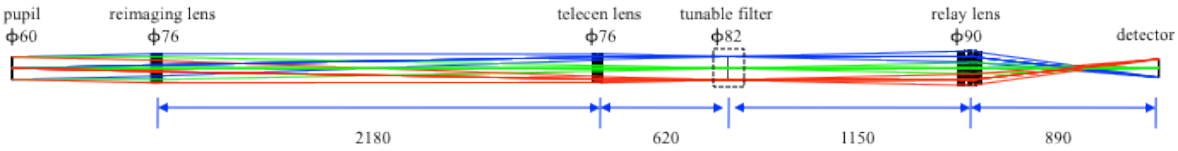

Fig. 2.19. Optical configuration of the narrow-band imager in the case when the Lyot filter is located at the telecentric beam of F/40.

Table 2.15. Basic parameters of the narrow-band imager.

Entrance pupil	60 mm
Telecentric beam	~F/40 (in the case of a Lyot filter) ~F/200 (in the case of a air-gap Fabry-Perot)
Focal length	1980 mm (F/33)
Detector size	4096 x 4096, 12μm/pixel
Pixel scale	0.05 arcsec /pixel
FOV	205 arcsec x 205 arcsec (1) 120 arcsec x 120 arcsec (2) 90 arcsec x 90 arcsec (3)

Pass-bands	517 nm	589 nm	630 nm	656 nm	854 nm
Spectrum lines	Mg I b	Na I D	Fe I	H I α	Ca II

(1) The optical configuration allows us to observe the FOV if the TF is big enough to cover the FOV.
(2) The FOV is available when the diameter of the Lyot filter is 50 mm φ at the F/40 telecentric focus.
(3) The FOV is available when the diameter of the Fabry-Perot filter is 180 mm φ at the F/200 telecentric focus.

Table 2.16. Requirements on TF.

wavelength range	500 – 870 nm
band width	~100 mÅ
Strehl ratio	>0.9
FOV	~200 arcsec
free spectral range	> 3 Å
tuning range	±3 Å
tuning speed	<5 s to scan FSR
tuning resolution	<5 mÅ
repeatability	<2 mÅ
uniformity	
wavelength	5 mÅ (TBD)
transmission	5 %
Stability	
wavelength	5 mÅ /day
transmission	1% /day
Parastic light	<2 %
Ghost	<1 %

2.7. Image stabilization system

In order to achieve high spatial resolution and precise polarimetric measurements in SUVIT of SOLAR-C, it is essential to achieve stable pointing of the telescope for solar images exposed on the detectors (see section 5.4 for more details). The image stabilization system (ISS) is to be implemented inside the telescope to reduce image displacements caused by attitude jitters of the spacecraft and disturbances generated by moving components (e.g. filter wheels, shutters, etc.). ISS consists of a correlation tracker (CT), which is installed in the spectrograph package and calculates image displacements by correlation tracking of solar granules, and a tip-tilt mirror (TM) to compensate the displacements, and servo control electronics. One of the mirrors in the collimator mirror unit (CMU) is to be used as the TM inside the SUVIT-OTA while the CT is to be installed in one of the focal plane packages, likely in the spectrograph package, because it is required to control behavior of the image stabilization system in coordination with slit-scanning observations of the spectro-polarimeter.

In HINODE SOT, we have developed ISS to remove residual pointing errors that the attitude control system cannot suppress in the frequency range lower than 14 Hz (Fig. 2.20 *left*), and achieved the pointing stability of 0.03 arcsec (3σ) as in-flight performance (Shimizu et al. 2008). It is expected to achieve better stability than 0.015 arcsec (3σ) in SOLAR-C SUVIT for the spatial resolution better than 0.1" and for the high polarimetric accuracy because pointing fluctuation during the polarization modulation introduces artificial polarization signals. High frequency disturbances induced by moving components and structural resonances are to be partially suppressed by extending the control bandwidth of ISS from 14Hz to about 100Hz (Table 2.17). It is a key to make use of a high-speed (faster than 5000 frames per second) camera with a CMOS device for correlation tracking of granule patterns. The simulated performance of ISS is shown in Fig. 2.20 (*right*).

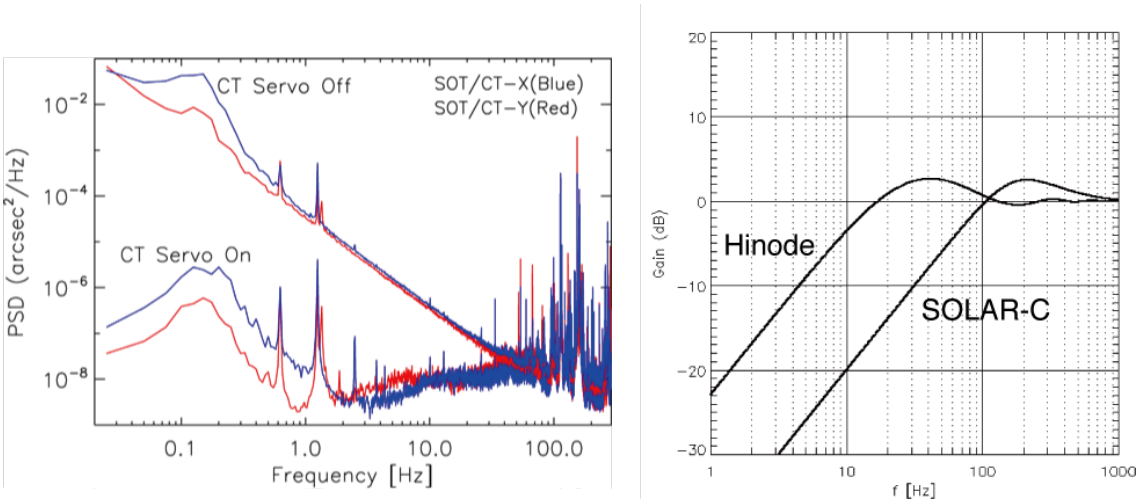

Fig. 2.20. Power spectrum densities of the pointing error signals measured with the CT in SOT (*left*). Simulated reduction performance of pointing error against input disturbances in SOLAR-C with the parameters given in Table 2.17 (*right*).

Table 2.17. Basic parameters of the servo-loop performance of ISS.

	HINODE SOT	SOLAR-C SUVIT
Cross-over frequency	14 Hz	> 100 Hz
Time const of TM drive	7.24×10^{-4} sec	$< 5 \times 10^{-4}$ sec
CT signal delay time	3.2×10^{-3} sec	$< 2 \times 10^{-4}$ sec

2.8. Contamination control

The contamination of the optical components becomes critical to carry out an observation in the UV wavelength range shorter than 400 nm. In the HINODE/SOT, gradual degradation of the throughput has been observed through its mission period. The degradation is supposed to be because of accumulation of molecular contaminants, which are out-gassed from organic components inside the telescope, on the surfaces of the primary mirror or the collimator lens unit. The decrease of the throughput is about 40% at 388 nm and about 50% at 396 nm 3 years after the launch. The corresponding throughput degradation at 280 nm is roughly estimated as ~20% if we scale an absorption coefficient of the contaminants to the shorter wavelength. In order to keep higher throughput in UV through the mission period, it is required to have more careful control of contamination environment in designing and developing the telescope. One possibility is to extend the period of bake-out of components in a vacuum chamber.

2.9. Integration and test plan

2.9.1. Integration and initial M1-M2 alignment

The SUVIT-OTA optical components are assembled in a dedicated integration and test tower structure having a dummy optical bench unit (OBU) that simulates a mounting interface of the spacecraft. The tower structure is capable of tilting the OTA from a vertical to horizontal configuration as well as rotating around the optical axis (Fig. 2.21). The integration is performed in the vertical configuration. After the CFRP truss structure is installed on the dummy OBU, M1 is installed on the mirror cell and its optical axis is aligned to the center of the mirror cell and the vertical line. Next, the ring plate assembled with the M2 and HDM units is installed on the top ring.

Then the OTA is tilted to the horizontal configuration. De-center, tilt and de-space of M2 with respect to M1 is adjusted using a Shack-Hartmann sensor attached to the mirror cell. The sensor can yield real-time coefficients of low-order Zernike polynomials such as focus (A20), primary astigmatism (A22, B22), coma (A31, B31) and spherical (A40) aberration. A high-precision folding flat mirror is set in front of the OTA entrance aperture. The Shack-Hartmann sensor is focused at the center of the secondary field stop, and the defocus and coma aberration is eliminated by adjusting positions and tilt of M2.

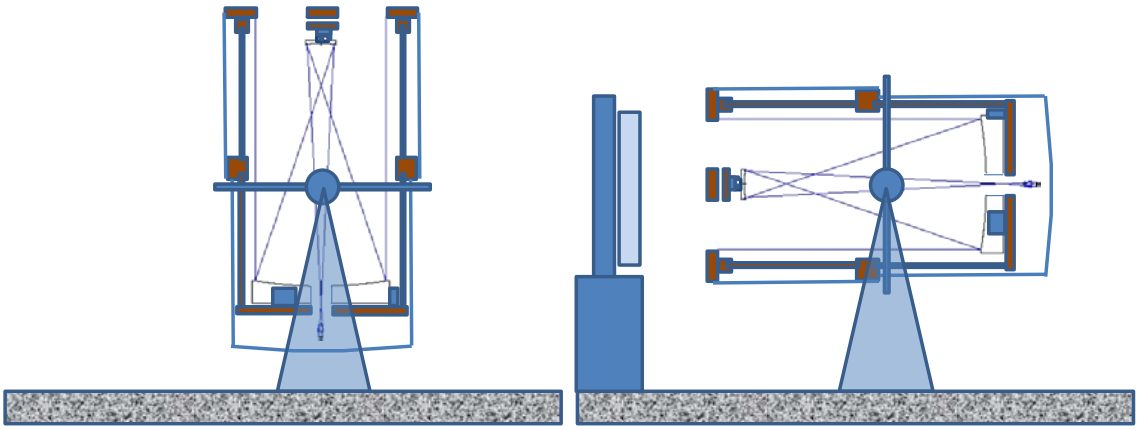

Fig. 2.21. OTA vertical configuration for telescope integration (*left*) and horizontal configuration for initial M1-M2 alignment with a Shack-Hartmann sensor and for optical performance test with an interferometer (*right*). By rotating the OTA around the optical axis in the horizontal configuration, it is possible to measure the wavefront error with canceling the gravity effect.

2.9.2. Zero-gravity optical performance test

The wavefront error of the OTA is measured in the horizontal configuration (+1 G condition) with an interferometer after integrating the CMU to the OTA. The interferometer sent a collimated beam into the OTA from the exit pupil. With the folding flat ahead the entrance pupil, the double-path wavefront error of the OTA is obtained. Next, rotating the OTA 180 degrees around the optical axis and setting the interferometer in the opposite side, the measurements for -1 G condition is performed. Averaging the -1 G and the +1 G wavefront errors can canceled out the effect of gravity. We can thus measure the wavefront error in the zero-gravity condition.

2.9.3. Opto-thermal test

The thermal model predicts that the OTA on orbit will inevitably have a large temperature gradient along the optical axis; the bottom part of telescope including M1 will reach a temperature from room temperature to higher than 50 ℃, while the upper structures supporting M2 will reach a temperature of 0 to 30 (TBD), depending on thermal conditions and its life phase. It is absolutely necessary, therefore, to verify the optical performance in such a temperature distribution even though the opto-mechanical design predicts that those temperatures are acceptable.

We will conduct opto-thermal testing of the OTA using a vacuum chamber dedicated for space environment tests of optical sensors. The configuration of the test setup is shown in Fig. 2.22. The OTA is mounted in a vacuum chamber in a horizontal configuration with a dummy OBU made of superinvar, and the folding flat mirror with a tilt and rotational stage is installed at one end of the chamber. Mounted on the side wall of the chamber, the interferometer looks into the OTA through an optical quality window. The vacuum chamber has upper and lower shrouds surrounding the entire OTA. By controlling temperatures of the shrouds, we can change the temperatures of upper and lower parts of the OTA independently, while the temperature of the folding flat mirror is always kept about the room temperature, using another temperature-controlled shroud.

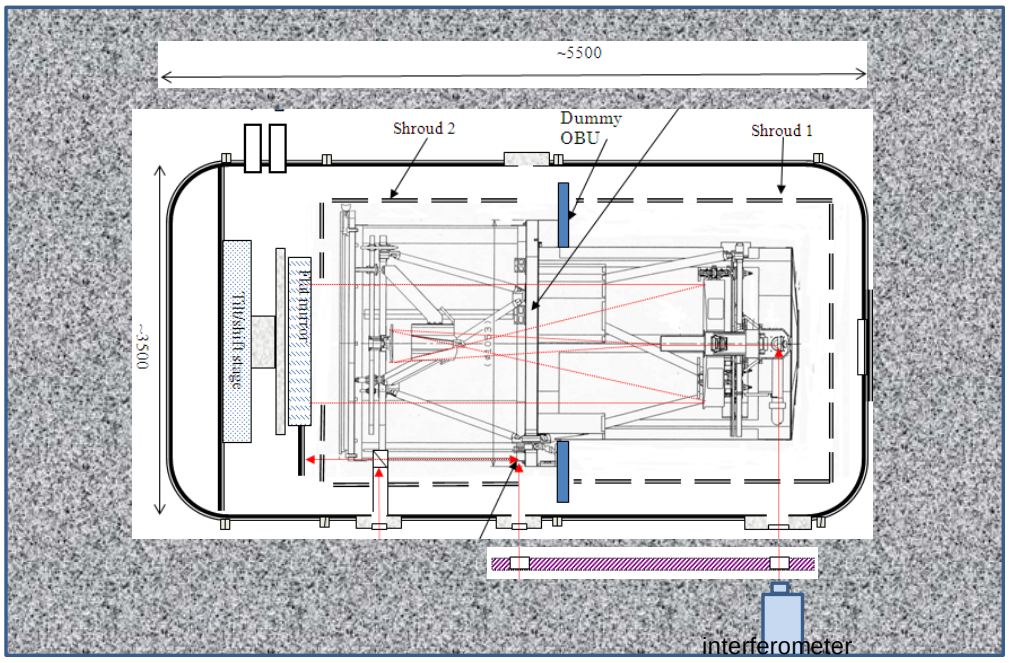

Fig. 2.22. Configuration to the OTA opto-thermal test.

Appendix A. Diagnostics of dynamics and magnetic fields in the chromosphere

A.1. Limitations in the Zeeman diagnostics

The only way to obtain quantitative information on magnetic fields in the solar atmosphere is via the measurement and physical interpretation of the emergent spectral line polarization. The approach commonly used is to analyze polarized line profiles due to the Zeeman effect. The polarization of the Zeeman effect is due to splitting of a spectral line in wavelength. An observational signature of the circular polarization produced by the longitudinal Zeeman effect is an anti-symmetric profile whose amplitude scales with the ratio, *R*, between the Zeeman splitting and the Doppler broadened line width.

$$R = \frac{1.4 \times 10^{-7} g_{eff} \lambda B}{\sqrt{1.663 \times 10^{-2} T / \mu + \xi^2}} \quad (1)$$

where g_{eff} is the effective Lande factor of the transition, μ is the atomic weight of the atom under consideration and λ is in Å, B in gauss, T in K and the non-thermal velocity ξ in km s^{-1}. The linear polarization amplitudes of the transverse Zeeman effect scale instead as R^2. The Zeeman effect produces significant amplitude of polarization when the line splitting is comparable with the line width, i.e. R~1, which is the case of photospheric lines. On the other hand, the Zeeman splitting is typically much smaller than the line width (i.e. R<<1) at the major chromospheric lines, because of relatively weaker field strength and larger line width in the chromosphere. This makes polarization amplitude smaller there especially in the linear polarization to obtain the transverse component of magnetic fields (Table 2.1 and Fig. 2.23). This is why we need high polarimetric sensitivity to diagnose magnetic field in the chromosphere.

A.2. Prospects of the Hanle diagnostics

There is another physical mechanism by means of which the magnetic fields of the solar atmosphere makes polarization of the emergent spectral line radiation: the Hanle effect. Anisotropic radiation pumping processes produce atomic level polarization (i.e., population imbalances and quantum coherences among the magnetic sublevels pertaining to any given degenerate energy level). The Hanle effect can be defined as any modification of the atomic level polarization due to the presence of a magnetic field. The Hanle effect makes changes in the polarized line profiles at magnetic strengths between ~$0.1B_H$ and ~$10B_H$ (Fig. 2.23), where the critical Hanle field strength (B_H, in gauss) is that for which the Zeeman splitting of the energy level under consideration is similar to its natural width:

$$B_H = 1.137 \times 10^{-7} / t_{life} g_J \quad (2)$$

with g_J the level's Landé factor and t_{life} its radiative lifetime in seconds. The critical Hanle field strength is typically from 1mG to 10 G dependent on the spectrum lines. This means that the Hanle effect is sensitive to weaker magnetic fields than the Zeeman effect (from at least 1 mG to 100 G), regardless of how large the line width due to Doppler broadening is. When the magnetic field is much stronger than the critical Hanle strength, the polarization amplitude does not depend on the field strength

(so-called Hanle saturation regime). Note that in the saturation regime the linear polarization signals created by atomic level polarization are still sensitive to the magnetic field orientation. When the field strength is strong enough, the linear polarization of chromospheric lines is generally due to the Hanle and transverse Zeeman effect (Fig. 2.23). Note also the circular polarization is always dominated by the longitudinal Zeeman effect, and the amplitude of the circular polarization provides information of the longitudinal field. The Hanle effect as a diagnostic tool is not limited to a narrow solar limb zone. In particular, in the forward scattering geometry of a solar disk center observation, the Hanle effect creates measurable linear polarization in the presence of an inclined magnetic field (Trujillo Bueno et al. 2002).

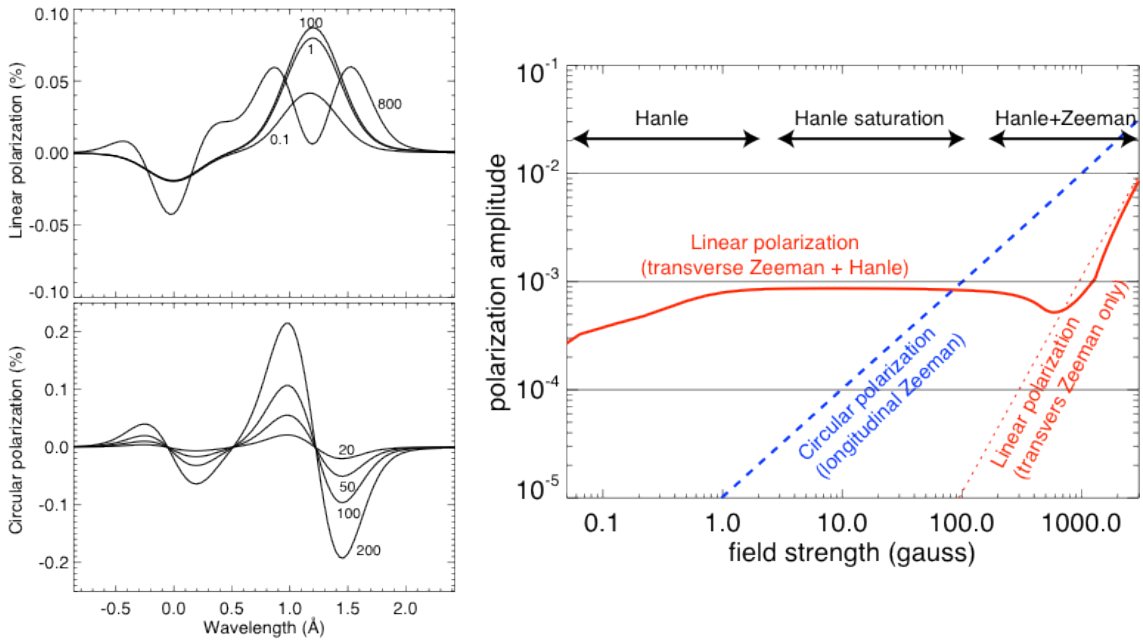

Fig. 2.23. (Left) Polarized spectrum line profiles at the He I 10830 Å for several field strengths (in gauss). The critical Hanle field strength B_H is about 0.8 gauss at the line. (Right) Polarization amplitude induced by joint action of the Zeeman and Hanle effect at He I 10830 Å as a function of the field strength (right). This is the case of forward scattering at the disk center and when the magnetic field is purely horizontal (for the linear polarization) or purely vertical (for the circular polarization). The Hanle effect allows us to diagnose transverse fields weaker than 100 gauss, which is not accessible with the transverse Zeeman effect only.

A.3. Inversion of chromospheric lines

The plasma velocities, temperatures, magnetic field vectors, and other interesting physical conditions in the solar atmosphere are not directly observable. In order to extract quantitative information on such conditions we need to make use of our knowledge on how the properties of the light are transformed as it propagates. A typical approach involves a non-linear fitting of observations of intensity and polarized spectrum profiles with synthetic ones obtained by solving the forward problem (i.e. radiative transfer) in a model atmosphere involving some unknown parameters. Because the chromosphere consists of complex fine structures organized by magnetic fields,

interpretation of chromospheric spectral lines requires simplification to restrict the number of unknown parameters that an observed line profile depends on.

A.3.1. Obtaining velocities and plasma parameters

One of the traditional methods to retrieve plasma parameters of chromospheric fine structures is so-called cloud modeling which describes the transfer of radiation through structures located higher up from the solar photosphere resembling clouds on earth's sky. Such cloud-like structures, when observed from above, absorb the radiation coming from below. The intensity line profiles mostly depends on transparency of the cloud to the incident radiation and also on the physical parameters in the cloud. Thus, in its most basic form cloud modeling delivers the four parameters, cloud optical thickness, cloud source function, cloud Dopplershift (i.e. velocity), and cloud Dopplerwidth, all four for a homogeneous cloud irradiated from below (see review by Tziotziou et al. 2007). The cloud source function can be converted into density and temperature through non-LTE calculation (e.g. Beckers 1972, Tsiropoula and Schmieder 1997) including static ionization equilibrium. Recent MHD simulations have shown that in chromosphere structures that suffer repetitive episodic heating, the actual populations of the atomic levels can be far from time-independent statistical equilibrium (Leenaarts et al. 2007). It is important to refine the cloud modeling to include time-dependent ionization as well as to compare data directly with numerical spectral line synthesis employing MHD simulations of time-dependent chromospheric structures.

A.3.2. Obtaining magnetic fields

Inversions of polarized Stokes profiles for photospheric lines have been developed and used routinely for over 20 years now to produce magnetic field maps. The simplest one is to use the Milne-Eddington method (e.g. Skumanich and Lites 1987) employing simplified assumption that all the physical parameters are constant in the line-formation region (except for the source function which varies linearly with optical depth) and has the advantage that the forward problem has an analytical solution, which makes the inversion robust and fast. The second method, the Stokes inversion based on response function (SIR, Ruiz Cobo and del Toro Iniesta 1992), is based on a full solution of the polarized LTE transfer in an arbitrarily one-dimensional atmosphere. It has the advantage that it is possible to determine the variation of physical parameters along the line of sight.

Similar tools for chromospheric inversions already exist and significant experience has been accumulated for nearly a decade now. There are several reasons why the analysis of chromospheric lines is more challenging. The biggest issue is that the radiative transfer in the chromosphere is non-LTE and there is not a universal solution. One needs to employ different techniques depending on the particular physical scenario under study (whether the polarization is originated by Zeeman effect or scattering, etc). They fall roughly into two different approaches. The He I triplet at 1083 nm forms over a very thin atmospheric slab because it forms by recombination of He II ions created by UV coronal illumination. The line formation allows us to use the Milne-Eddington type of approach as a valid approximation to derive accurate magnetic fields in the Zeeman regime (Lagg et al. 2004). The inversion code HAZEL (Hanle and Zeeman Light,

Asensio Ramos, Trujillo Bueno & Landi Degl'Innocenti 2008) is able to tackle the full problem including the Zeeman and Hanle effects self-consistently in such a slab (Fig. 2.24).

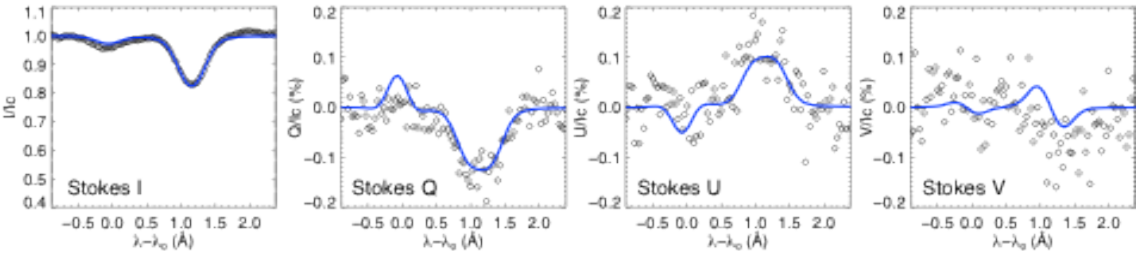

Fig. 2.24. Example of a spectro-polarimetric observation of He I 10830 Å line and non-linear fitting of the observed line profiles with HAZEL.

Another alternative is the generalization of SIR to non-LTE atmosphere (Socas-Navarro et al. 1998). In the current code, the polarization generation is restricted to the Zeeman regime only but the line formation is treated fully in non-LTE, with the assumptions of instantaneous ionization equilibrium and complete angle and frequency redistribution (CRD). The CRD approximation is valid for some lines such as those in the Ca II infrared triplet at around 850 nm (Uitenbroek 1989). The non-LTE inversion was successfully applied to spectro-polarimetric observations in the Ca II infrared triplet to get three-dimensional magnetic structures around a sunspot (Socas-Navarro et al. 2005). The validity of the inversion and the possible impact of ionization history and three-dimensional radiative transfer are currently been studied using numerical MHD simulations of the chromosphere (de la Cruz Rodriguez et al. 2010, Fig. 2.25) though these approximations affect only the determination of thermodynamical parameters but not the magnetic field vector and the line-of-sight velocity.

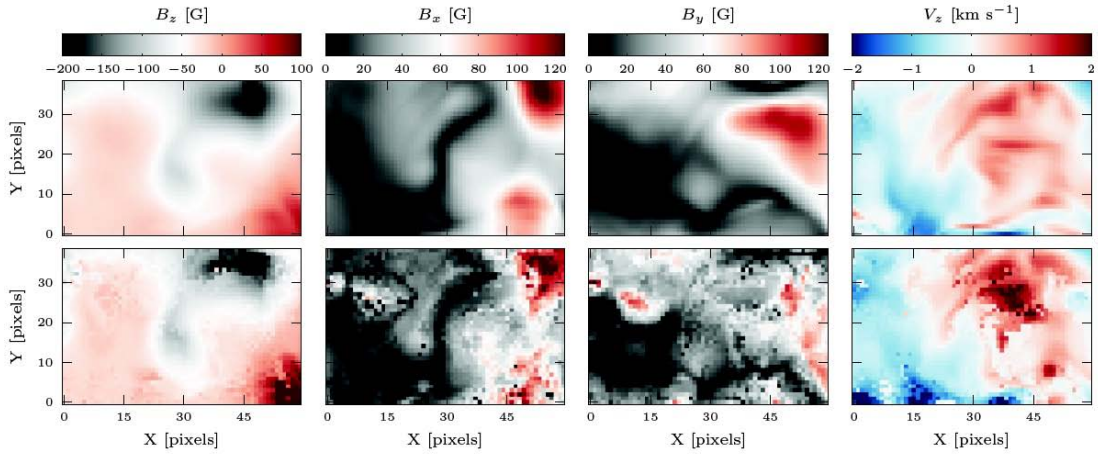

Fig. 2.25. Test of the non-LTE inversion in the Ca II 854 nm line using the numerical MHD simulation of the chromosphere (see A.4), where top panels show parameters from the simulation and bottom panels show parameters obtained with the inversion of the synthesized line profiles.

Because the non-LTE inversion requires lots of computational power, it is under investigation to apply pattern recognition techniques such as principal component

analysis (PCA, Casini et al. 2005) and artificial neural network (ANN, Socas-Navarro 2005) to the inversion of the chromospheric lines. The general idea behind the pattern-recognition approach is to create a sufficiently dense and uniform database of magnetic and atmospheric models that are relevant for the line formation characteristics in an observation. The computationally intensive forward-model step is thus pushed upfront to a one-time calculation of an adequate database of Stokes profiles, while the inversion problem is reduced to the search in that database of the best match to the observed line profiles.

A.4. Numerical modeling of the chromosphere

In order to fully exploit detailed chromospheric line observations, including their polarization measurements, a promising approach would incorporate comparisons of observed spectral line properties and dynamic phenomena with those seen in numerical MHD simulations of the same observables. This requires 3D models of the photosphere and the chromosphere including a realistic description of the important physics. From such models it is then necessary to calculate the observable spectral lines employing radiative transfer.

Although there are lots of complexities in the modeling, several codes exist within the description of single-fluid magnetohydrodynamics. They can treat the detailed radiative transfer, and their photospheric simulations reproduce detailed observations to remarkable detail (e.g. Stein and Nordlund 2006). In the chromosphere, scattering starts to play an important role, radiative losses in strong lines from calcium, magnesium and hydrogen, where non-LTE is crucial, and the hydrogen ionization balance is out of statistical equilibrium. Recently numerical codes have been developed that can treat all these effects and simulations have been produced where comparisons with observations start to become meaningful (Fig. 2.26, e.g. Leenaarts et al. 2009). Efforts are also underway to go beyond the single-fluid magnetohydrodynamic description of the chromosphere.

Once a realistic simulation exists it is necessary to calculate the observable radiation in order to compare with the observations. It is important that the employed radiative transfer codes are capable of handling partial frequency redistribution (PRD), which accounts for the coherence of the incoming and outgoing photons in scattering events in strong chromospheric spectral lines like the Mg II h/k and the Ca II H/K lines. In addition, to compare with observations of polarization in chromospheric lines, the radiative transfer codes should be able to calculate polarized line profiles from a given three-dimensional magnetic configuration in an MHD simulation. Several non-LTE transfer codes already exist that meet many of the requirements, and in the near future these efforts will be combined.

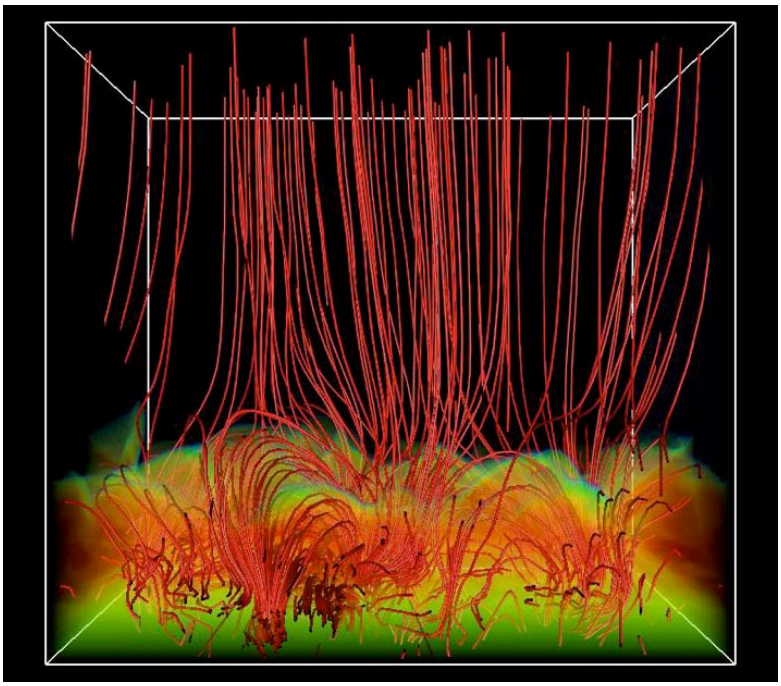

Fig. 2.26. Snapshot of a 3D radiative MHD simulation including the photosphere, chromosphere, and corona (courtesy of Carlsson and Hansteen).